Politecnico di Torino

Master's Degree in Aerospace Engineering

Vibroacoustic analysis of laminated sandwich panels for space applications

Supervisor:
Prof. Alfonso Pagani
Co-Supervisors:
Ing. Piero Chiaia
Prof. Matteo Filippi

Candidate:
Gaia Littera

Academic Year 2023-2024

Bastava imparare a guardare oltre le stelle più lontane.

Acknowledgements

I wish to express my deepest gratitude to my supervisor, Prof. Alfonso Pagani, for granting me the opportunity to explore such a challenging and stimulating research.
I am equally thankful to my co-supervisors, Piero Chiaia and Matteo Filippi, for their constructive feedback and support, which enhanced the quality of this work. Additionally, I would like to extend my appreciation to my family and friends for their encouragement and support during this journey.

Abstract

This thesis presents a comprehensive vibroacoustic analysis of laminated sandwich panels designed for space applications, focusing on their structural and acoustic performance. The primary objective of this research is to assess the dynamic behavior of these panels using static, modal, and dynamic analyses. To achieve this, a high-order plate finite element model is employed, with simulations performed using the MUL2 code developed at Politecnico di Torino, accurately representing the complex mechanical characteristics of the sandwich structures.

The dynamic response of representative laminated sandwich plates is analyzed, with modal analysis highlighting key vibrational modes. The results of the dynamic analysis are presented in terms of the Power Spectral Density (PSD) of displacements, stresses, and strains. A detailed Sound Pressure Level (SPL) analysis is also conducted, providing critical insight into the acoustic radiation properties of the panels, which is essential for assessing their performance in noise-sensitive aerospace environments.

The results reveal distinct vibrational characteristics and acoustic behavior, providing valuable insights into optimizing the design of laminated sandwich panels for space structures. These findings contribute to both the structural integrity and acoustic performance of aerospace applications, ensuring reliability during the demanding launch phase and operation in space environments.

Acronyms

ASD Acceleration Spectral Density. 15, 19

CFRP Carbon Fiber-Reinforced Plastic. 35, 63, 64

CLA Coupled Loads Analysis. 26

CPT Classical Plate Theory. 42

CUF Carrera Unified Formulation. 39, 41, 43, 46

DFAN Direct Field Acoustic Noise. 23, 24

DOF Degrees of Freedom. 57, 58, 67, 80, 82

ESA European Space Agency. 27

ESL Equivalent Single Layer models. 49, 50

FE Finite Element. 67, 82

FEA Finite Element Analysis. 72

FEM Finite Element Method. 35, 39, 44, 46, 72, 80

FN Fundamental Nuclei. 39

FRF Frequency Response Function. 15, 79

FSDT First-Order Shear Deformation Theory. 42

GRFP Glass Fibre-Reinforced Plastic. 34, 63

LW Layer Wise. 51

MPE Maximum Predicted Environment. 18, 19

OASPL Overall Sound Pressure Level. 4

Contents

List of Figures

List of Tables

Chapter 1

Introduction

In space applications, structural components are exposed to severe acoustic and vibrational environments, particularly during the launch phase. The combined effects of propulsion systems and aerodynamic pressures generate intense noise and vibrations, which can lead to undesirable responses such as deflections, fatigue, or even failure, especially when lightweight materials are employed.

To address these challenges and meet the demands of modern space missions, innovative materials and design strategies have been developed. Among these, laminated honeycomb sandwich panels stand out for their remarkable strength-to-weight ratio and their ability to damp vibrations effectively. These properties make them a great solution in spacecraft structures, such as satellite bodies and payload fairings, where reducing weight without compromising structural integrity is essential for performance and reliability under various and critical conditions.

In the design of aerospace structures, accurately predicting the complex structural behavior of these materials, such as instabilities, localized phenomena, and potential failure, is paramount. While physical testing of such components is essential, it often proves to be costly, time-consuming, and practically challenging, particularly when dealing with innovative materials and structures. Tests such as those conducted in a Reverberant Chamber, which simulate the acoustic and vibrational environments encountered during launch, are valuable but difficult to perform repeatedly due to their high costs and the complexity of setup. In this context, alternative approaches like DFAN testing offer a more

cost-effective means of assessing the acoustic performance of these structures under realistic conditions.

These challenges highlight the need for computational methods to assess the performance of these complex structures. Consequently, numerical simulations emerge as a powerful alternative to physical testing. In particular, the Finite Element Method (FEM) has become an invaluable tool, as it allows for detailed investigations of static, dynamic, and acoustic responses, providing accurate predictions of material behavior under various loading conditions. This computational approach enables the analysis of phenomena that are often inaccessible through experiments alone, such as large displacements, vibrations, and progressive failure.

This thesis focuses on the mechanical, dynamic, and vibroacoustic analysis of laminated plates for space applications. The primary objective is to understand how these panels behave under various vibrational and acoustic loads, assessing their performance across a wide frequency range, employing a numerical model that can accurately describe the dynamic behavior of these structures. In the present thesis, high-order 2D plate Finite Element (FE) models are presented in the well-established Carrera Unified Formulation (CUF) framework.

The work is organized as follows:

- Chapter 2 delves into the fundamental concepts of the acoustic and vibrational environment faced by space structures, including the types of noise encountered during spacecraft operation. It outlines the motivation for the study and the elevance of vibracoustic analysis.

- Chapter 3 introduces the experimental methodologies and testing procedures used for vibro-acoustic analysis.

- Chapter 4 outlines how sandwich honeycomb structures can be an innovative solutions to modern spacecraft design, and delves into the design and materials of sandwich panels, covering the different core setup (such as honeycomb and foam), and core and face sheet materials commonly

used in aerospace. Also, some analytical models for the equivalent and effective material properties are presented.

- Chapter 5 presents the computational model, based on FE procedures, to solve the pure mechanical problem and the vibroacoustic analysis of multilayered plate structures. The governing equations are written under an energetic approach, exploiting the Principle of Virtual Displacements (PVD) to carry out the weak-form equilibrium equations. An high-order 2D plate model is considered, defined in the well-established CUF framework, developing an efficient finite element procedure for the analysis of multilayered structures with complex structural properties. Under this formulation, both Equivalent-Single-Layer (Equivalent Single Layer models (ESL)m) and Layer-Wise (Layer Wise (LW)m) models are taken into account through a compact and hierarchical approach.

- Chapter 6 is dedicated to the static analysis of laminated panels, focusing on assessing the capabilities of the developed computational models in representing the static behavior of these structures under various loading conditions. This evaluation includes a detailed study of multi-layered plates, laminated soft-core sandwich panels, and laminated aluminium honeycomb sandwich plate with CFRP skins, ensuring that the models are accurate and reliable. The validation performed in this chapter is specifically aimed at preparing the models for subsequent vibroacoustic analyses, confirming their suitability for predicting dynamic responses.

- Chapter 7 deals with the modal analysis of sandwich panels, assessing the unperturbed modal behavior of these structures and the capabilities of the present FE approach. The results, discussed in terms of natural frequencies and mode shapes, gives more practical information on the influence of the material properties and boundary conditions applied.

- Chapter 8 delves into the frequency response analysis of plates using FE models. It focuses on the interplay between boundary constraints and pressure loads, which range from 8 Pa to 32 Pa, as a critical factor in understanding their dynamic behavior.

- Chapter 9 provides a detailed analysis of the SPL behavior of sandwich panels under various loading conditions, with a specific focus on modeling pressure loads and power spectral densities (PSDs).

Chapter 2

Acoustic Environment

During their life operations, spacecrafts experience various environmental conditions. The launch phase is particularly critical, as it exposes the structure to multiple intense loads, including aerodynamic forces, acoustic and and thrust-induced pressures. These combined effects can induce structural vibrations, which, if not properly managed, may result in failure or undesired responses, adversely affecting avionics and payloads, with potential implications for the overall success of the mission.

Modern spacecraft design demands that structures withstand these severe conditions while maintaining their nominal performance standards. Vibrations, in particular, require careful consideration during the design phase, as they play a pivotal role in determining structural integrity and the proper functioning of systems. This underscores the necessity of a detailed analysis of the dynamic properties of spacecraft structures to ensure their resilience and performance under operational stresses.

This chapter provides an overview of the acoustic and vibrational environments encountered during the launch phase, presenting findings from the literature review. It introduces the vibroacoustic problem by highlighting the key challenges posed by structural vibrations and their impact on spacecraft reliability during critical mission phases.

2.1 Acoustic Performance Metrics

In spacecraft design, understanding and managing acoustic performance is crucial due to the intense sound environments encountered during launch and operation. Acoustic performance metrics provide essential data to ensure that spacecraft structures and systems can withstand and function effectively under these demanding conditions.

One of the key metrics is the Sound Pressure Level (SPL). The SPL quantifies the intensity of sound and it reflects how loud the noise is relative to a standard reference pressure. The SPL over the spectrum of frequencies at which the pressure can fluctuate is expressed in dB and defined as:

$$\text{SPL} = 10 log \frac{P^2}{P_{ref}^2} = 20 log \frac{P}{P_{ref}}, \tag{2.1}$$

where P is measured in Pascals (Pa) or Decibel (dB), and P_{ref} is the audible limit of the human ear, with a value of 2×10^{-5} Pa or $120 dB$.

The acoustic environment is not generally provided at each and every frequency but it is usually expressed by a 1/3-octave-band pressure spectrum for center frequencies. The frequency band for 1/3-octave-band signal is defined as:

$$\Delta f(f) = \left(2^{\frac{1}{6}} - 2^{-\frac{1}{6}}\right)f = 0.2316f. \tag{2.2}$$

The fluctuating pressures associated with acoustic energy during launch can cause vibrations of structural components over a wide frequency range. Therefore, the center frequenciy f will range from about $20 Hz$ up to $10000 Hz$ [1]. These high-frequency vibrations can rapidly induce structural fatigue.

When pressure levels are defined, it is convenient to provide through the Overall Sound Pressure Level (OASPL) a measure of the overall acoustic noise intensity. OASPL can be determined from 1/3 octave band data as the deci-

bel representation of the root-sum-square p_{rms} of the pressure levels.

$$p_{\text{rms}} = \sqrt{\frac{1}{T} \int_0^T p^2(t)\, dt} \qquad (2.3)$$

$$\text{OASPL} = 20 \log_{10} \left(\frac{p_{\text{rms}}}{p_0} \right) \qquad (2.4)$$

Another relevant metric is the Sound Transmission Loss (STL). The STL is an "*index used to describe the amount of sound reduction, in dB units, that a partition imparts to the transmitted acoustic wave for a given incident field*" [2]:

$$STL = 10 \log \frac{1}{\tau} = 10 \log \left(\frac{I_i}{I_t} \right), \qquad (2.5)$$

where τ is the sound transmission coefficient, I_i is the incident sound intensity, and I_t is the transmitted sound intensity. To improve the sound insulation performance, materials with higher mass density and flexural rigidity are preferred [2].

2.2 Acoustic and Vibration Sources in Spacecraft Operations

There are numerous environmental conditions and sources of vibration during the different operational phases of a spacecraft. As shown in Table 2.1, harsh vibration can result from thrust oscillation, rocket-engine resonances, wind gusts and shear, transportation, testing, operation of internal equipment, pyrotechnic devices used to separate the stages of the launcher, and unstable dynamic coupling of the structure with the control or propulsion systems.
However, at the integrated spacecraft level, *acoustic noise* is a primary source of vibration excitation [4].

Figure 2.1 offers a compelling visualization of the extreme acoustic pressures experienced during a rocket launch [5].
The decibel scale illustrates the significant increase in noise levels from the quieter regions of the payload fairing to the deafening intensity at the base

Operation	Phase	Source
Prelaunch	*Functional checkout*	Vibration testing Static firing
	Transportation	Air turbulence Propeller noise Rough highways Rough water
	Launch readiness	Ground wind
Launch	*Liftoff*	Ignition Engine noise Tie-down release
	Ascent	Engine roughness Aerodynamic noise and buffet Pogo phenomena Control-system instability
	Staging	Separation Stage ignition
Space	*On station*	Control-system instability
Atmospheric	*Entry*	Aerodynamic noise and buffet Aerodynamic stability

Table 2.1: Environmental conditions and sources of vibration during different operational phases of a spacecraft. [3]

of the vehicle and within the flame trench. The differentiation between *Ascent Acoustics* and *Abort Acoustics* underscores the dynamic nature of launch conditions and the importance of considering both normal and emergency scenarios when designing spacecraft and protective equipment for the the mission payload.

There are three primary dynamic environments [6]:

- The high-frequency acoustic pressure environment (5 to 10000 Hz), driven by engine noise during static firing and lift-off, as well as fluctuating in-flight pressure during transonic and supersonic phases of ascent and reentry.
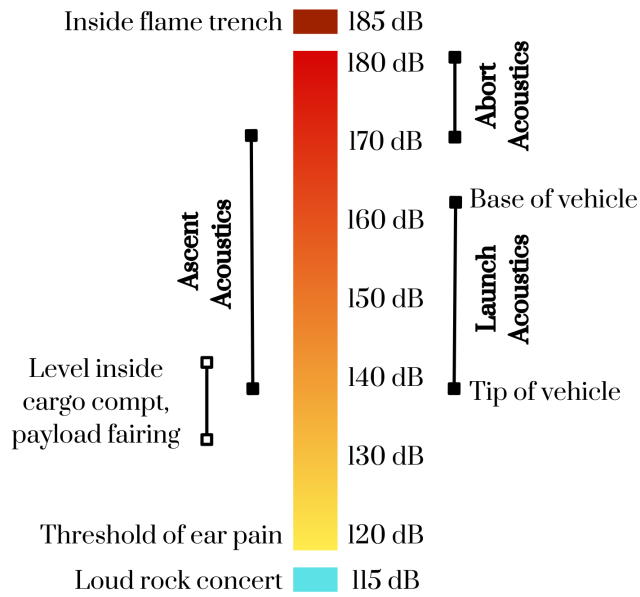
Figure 2.1: Surface pressure fluctuations on launch vehicles.

- The high-frequency random vibration environment (20 to 2000 Hz), induced by both mechanical and acoustic sources.

- The low-frequency vehicle transients (0 to 50 Hz), caused by events such as engine ignition, launch release, staging, parachute deployment, and landing.

2.2.1 Propulsion system noise

Rocket acoustic loads include quasi-static loads generated by thrust during steady engine burn, transient loads during engine ignition and shutdown, and acoustic loads produced by engine noise. The engines exhaust gases create turbulence, generating pressure fluctuations, that are transmitted as acoustic noise to the surroundings at the speed of sound. The acoustic noise and resulting structural vibrations are random as the turbulence that create them: smaller-scale mixing near the engine produce higher-frequency noise, while lower-frequency noise comes from larger-scale mixing further away[7]. However, the principal source of the noise is the subsonic flow, downstream of the supersonic core of the jet [7].

The acoustic sound power W_a generated by a supersonic rocket exhaust is directly proportional to the cube of the exhaust velocity u_e [7]. The total acoustic power W_a is related to the mechanical power W_m generated by the rocket by the expression [5]:

$$W_a = \eta W_m = \eta \sum_{\text{all nozzles}} \frac{1}{2} T u_e \qquad (2.6)$$

where T is the thrust and η is the efficiency factor (0.2-0.8%).
The spectrum of the noise is measured in Hertz and the peak frequency f_{peak} is inversely proportional to the size of the engine D [7].

$$f_{peak} \propto \frac{1}{D} \qquad (2.7)$$

Noise is emitted in all directions, with the greatest intensity occurring at an acute angle, typically between 50 and 70 degrees [7] from the axis of the exhaust flow (Figure 2.2).
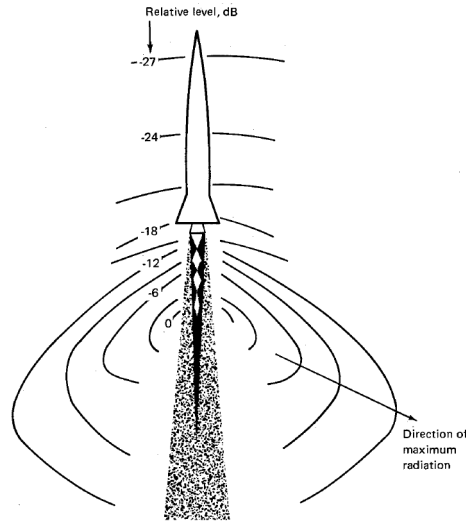
Figure 2.2: Rocket flow and contour of equal overall sound pressure level for in flight case [7].

The launch pad, surrounding terrain, and weather conditions can also influence the acoustic field by reflecting or shielding the sound to varying degrees (Figure 2.3). Indeed, acoustic load reduction is also accomplished by modifying the launch pad design. This involve adjustments to the shape of the flame deflector,

10

such as changing its angle, or developing movable adjustable launch platforms where the size and number of exhaust exit perforations can be varied [8]. The maximum possible reduction in acoustic loading to be sought in ground operation for vehicle-design purposes is on the order of 15 to 20 dB [7].
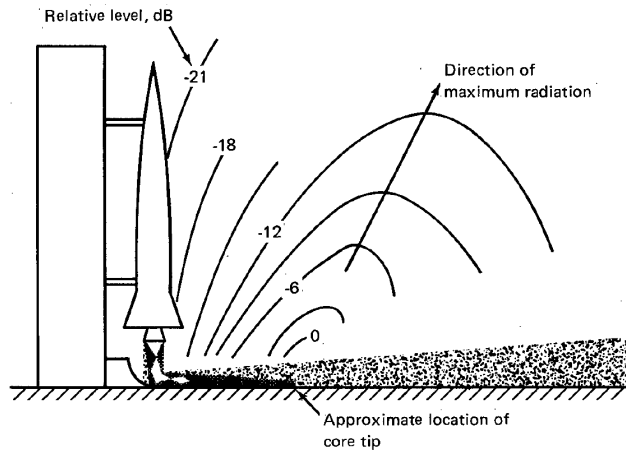
Figure 2.3: Rocket flow and contour of equal overall sound pressure level for launch case [7].

Another noise reduction techniques is the *injection of water* into the exhaust stream. Water injection reduces noise through two primary mechanisms [8]:

1. It lowers the plume's mean velocity, reduces velocity fluctuations, and decreases turbulent shear stresses. This occurs as a result of momentum and heat transfer between the water and the plume, as well as the evaporation of water.

2. It scatters and absorbs acoustic waves through the presence of water vapor and droplets, and additionally provides acoustic insulation through the formation of a water curtain.

This combination of effects mitigates the noise generated in propulsion systems. However, the results show that this reduction method require large quantities of water and it is constrained by the launch platform design. These systems appear impractical for large boosters [7], but recent studies show a great noise reduction up to 6 dB [9] [10].

The acoustic loading on the vehicle can also be reduced by *design*. Inside the rocket-engine combustion chamber, acoustic resonances can occur due to the

mixing of propellant gases which produces fluctuating pressures on the engine wall (*Pogo oscillation*). These resonances are usually reduced or eliminated during engine design and development.

The choice of less-noisy rocket engines will not normally be possible since engine selection is determined by other requirements. However, a reduction can be achieved by choosing an engine with a lower exhaust velocity, which is determined by the *choice of propellants*. Solid rocket motors tend to be noisier because they have high exhaust velocities and high mass flow rates. Liquid rocket engines, such as those using liquid oxygen (LOX) with RP-1 (a refined form of kerosene) or liquid hydrogen (LH2), tend to be less noisy compared to solid rockets. Among liquid propellants, engines using LOX/LH2 are typically quieter than those using LOX/RP-1 due to the lower molecular weight of the exhaust gases and lower exhaust velocities.

2.2.2   Aerodynamic noise

As a space vehicle moves rapidly through the atmosphere, turbulence in the boundary layer generates pressure variations known as *aerodynamic noise* or *buffeting*, that induce structural vibrations. Changes in the vehicle's cross-sectional area create shock waves in the aerodynamic flow, increasing turbulence and fluctuating pressures. During launch and ascent, the vehicle's increasing speed in the transonic regime creates a transient pressure field, forming new unstable shock waves that cause structural vibrations. In the supersonic regime, shock waves are generally stable and less affected by speed or attitude changes, resulting in a more stationary fluctuating pressure field. The high-level acoustic noise environment continues during supersonic flight, generally until the maximum dynamic pressure is reached [11].

Chapter 3

Vibroacoustic Analysis Methods and Tests

3.1 Methods

The end goal of acoustic analysis is to predict structural responses due to acoustic loads. Various methods are available for determining structural integrity and predicting equipment-vibration requirements. These methods can be divided into three categories: *classical analysis*, *statistical energy analysis*, and *extrapolation*.

3.1.1 Classical Analysis

Classical (or *deterministic*) analyses involve representing the vehicle structure, or one of its components, with a *mathematical model*. In these type of analysis the applied load is described by its time history or *loading spectrum*, and spacial resolution [11].
There are two types of mathematical models: *continuous* or distributed parameter representations, and *lumped* or discrete parameter representations. The choice of the mathematical model depends on the required accuracy, frequency range, computational cost, and model formulation. For simple geometries (e.g. domes, conical and cylindrical shells, plates, and beams) and classical boundary conditions, a distributed representation is employed [11]. Instead composite constructions, complex boundaries, and structures with attached masses

can be analyzed adopting a lumped-parameter representation.
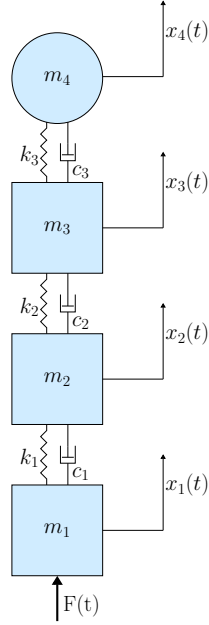
Figure 3.1: Typical lumped-parameter model of a space-vehicle.

The vibroacoustic problem is analyzed starting from the classical dynamical equation of motion of multi degrees-of-freedom system:

$$\mathbf{M}\ddot{x}(t) + \mathbf{C}\dot{x}(t) + \mathbf{K}x(t) = F(t) \tag{3.1}$$

where $\mathbf{M}$, $\mathbf{C}$, and $\mathbf{K}$ are the square matrices of mass, damping, and stiffness coefficients, respectively, while $\mathbf{x}$ and $\mathbf{F}$ are the vectors of displacement and applied forces.

To analyze the response of the payload fairing to vibrations introduced at its base, a single-degree-of-freedom system, with unit acceleration applied at the base of the spring, is considered [12].
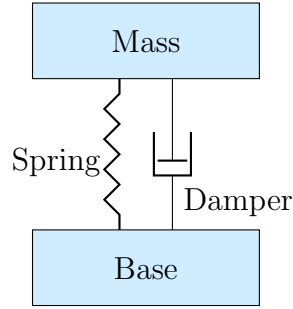
Figure 3.2: Mechanical system with a spring and damper.

The transmissibility function, $TR(f_{ratio})$, represents the peak response acceleration as a function of the ratio f_{ratio} between the input frequency, f, and the natural frequency, f_n, of the SDOF system.

$$TR(f_{\text{ratio}}) = \sqrt{\frac{1 + (2\zeta f_{ratio})^2}{(1 - f_{ratio}^2)^2 + (2\zeta f_{ratio})^2}} \qquad (3.2)$$

The damping ratio, denoted by ζ, is defined as the ratio of the actual damping factor to the critical damping factor.
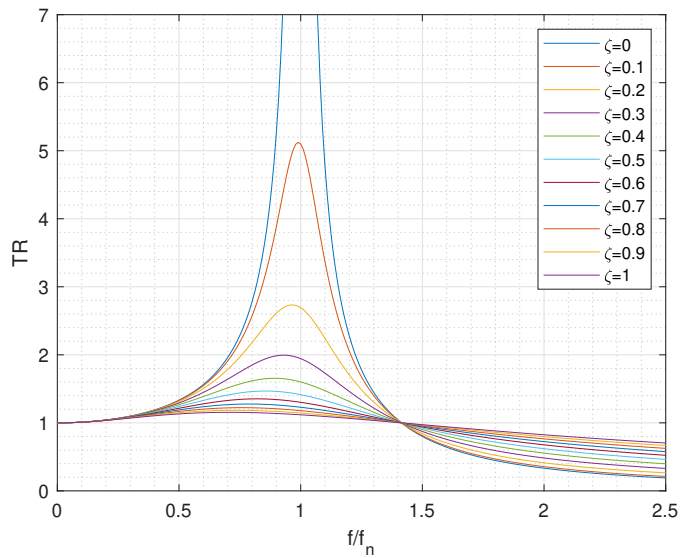
Figure 3.3: Transmissibility function.

Resonance occurs when the frequency of a continuous sinusoidal input matches the system's natural frequency. The system reaches an equilibrium where the energy added with each new cycle of input is balanced by the energy dissipated

15

through damping. As a result, the amplitude of the system's response at resonance is constrained by the level of damping present.

$$Q = \frac{1}{2\zeta} \tag{3.3}$$

The transmissibility at resonance is represented by the quality factor Q. When the forcing frequencies are much lower than the system's natural frequency, the mass closely tracks the motion of the mounting base, leading to minimal dynamic amplification. However, when the forcing frequency exceeds $\sqrt{2}$ times the natural frequency, the mass experiences less acceleration than the base. This behavior is called *isolation*.

Frequency Domain Analysis

Frequency domain analysis provides more information for applicable problems compared to its time domain counterpart. In linear time-invariant system of equations, if the external forces input $\mathbf{F}(t)$ can be represented as its harmonic expansion, also the output $\mathbf{x}(t)$, namely the displacements, can be represented with another harmonic expansion by means of the same frequencies. In a one-dimensional framework, let $\mathbf{F}(t)$ be the external forces, written as its *Fourier series expansion*:

$$F(t) = A_0 + \sum_{h=1}^{\infty} \left(A_h cos\frac{2\pi ht}{T} + B_h sin\frac{2\pi ht}{T} \right) \tag{3.4}$$

where A_0 is the mean value of the forcing function. A_h and B_h are defined by the Fourier coefficients:

$$A_0 = \frac{1}{T} \int_0^T F(t)dt \tag{3.5}$$

$$A_h = \frac{2}{T} \int_0^T F(t)cos\frac{2\pi ht}{T}dt \tag{3.6}$$

$$B_h = \frac{2}{T} \int_0^T F(t)sin\frac{2\pi ht}{T}dt \tag{3.7}$$

The dynamic response of the system is derived as a superposition of the differ-

ent contributions expressed in terms of a transfer function $H(f)$ or Frequency Response Function (FRF):

$$H(f) = 1 + \frac{(f/f_n)^2 \left(\left(1 - (f/f_n)^2\right) - j\left(\frac{f/f_n}{Q}\right) \right)}{\left(1 - (f/f_n)^2\right)^2 - \left(\frac{f/f_n}{Q}\right)} \tag{3.8}$$

where f, f_n and Q are the input frequency, the natural frequency and the quality factor, respectively. This transfer function describes the system's response to a harmonic input. Any response parameter can be obtained as the product of the input and an appropriate transfer function.

To introduce the definition of the PSD it is necessary to explicit the *Fourier transform*:

$$X(f) = \int_{-\infty}^{+\infty} x(t)e^{-j2\pi ft}dt \tag{3.9}$$

The PSD is the Fourier transform of the *autocorrelation function*, which describes how a function (such as the response or input base acceleration) correlates with itself over time. The PSD S_{xx} shows how the power of a generic signal $x(t)$ is distributed across different frequencies.

$$S_{xx}(\omega) = \int_{-\infty}^{+\infty} R_{xx}(t)e^{-i\omega t}dt \tag{3.10}$$

where R_{xx} is the autocorrelation function defined as:

$$R_{xx}(t) = \lim_{T \to +\infty} \frac{1}{T} \int_{-T/2}^{T/2} x(t) \cdot x(t + dt)dt \tag{3.11}$$

The term *spectral* in PSD refers to this frequency content. *Power* indicates the influence of each frequency component on the overall mean square value of $x(t)$. Lastly, *density* implies that frequencies are continuously distributed, meaning that the contribution of a frequency band between f and $(f + df)$, rather than a single frequency, is considered. If a structure is subjected to a

pressure load at its base, as in the case of the payload fairing shown in Fig.3.1, the equaton of motion, similar to Eq. 3.1, is the following:

$$m\ddot{x}(t) + c\dot{x}(t) + kx(t) = P(t) \tag{3.12}$$

where $c = 2m\zeta\omega_n$ and $\omega_n = 2\pi f_n = \sqrt{\frac{k}{m}}$.

$$\ddot{x}(t) + \frac{c}{m}\dot{x}(t) + \frac{k}{m}x(t) = \frac{1}{m}P(t) \tag{3.13}$$

The following equation is obtained,

$$\ddot{x}(t) + 4\pi\zeta f_n\dot{x}(t) + (2\pi f_n)^2 x(t) = \frac{1}{m}P(t) \tag{3.14}$$

Considering the Fourier transform of the left and right-hand side of Eq. 3.14,

$$-(2\pi f)^2 X(f) + (j2\pi f)4\pi\zeta f_n X(f) + (2\pi f)^2 X(f) = \frac{1}{m}P(f) \tag{3.15}$$

$$\ddot{X}(f) - j2\zeta(\frac{f_n}{f})\ddot{X}(f) - (\frac{f_n}{f})^2\ddot{X}(f) = \frac{1}{m}P(f) \tag{3.16}$$

it is possible to explicit the output in terms of acceleration:

$$\ddot{X}(f) = H(f)P(f) \tag{3.17}$$

$$W_a(f) = |H(f)|^2 W_p(f) \tag{3.18}$$

where $W_a(f)$ is the PSD of the acceleration, known also as Acceleration Spectral Density (ASD), $W_p(f)$ is the *Pressure Spectral Density*, and $H(f)$ is defined as:

$$H(f) = \frac{1}{m}\left(\frac{1}{1 - j2\zeta\left(\frac{f_n}{f}\right) - \left(\frac{f_n}{f}\right)^2}\right) \tag{3.19}$$

The *Pressure Spectral Density* can be defined as:

$$W_p(f) = \frac{P(f)^2}{\Delta f(f)} \tag{3.20}$$

where $P(f)$ is derived from Eq. 2.1:

$$P(f) = P_{ref}10^{SPL/20} \tag{3.21}$$

3.1.2 Statistical Energy Analysis

Since traditional methods often struggle to provide accurate or cost-effective results, especially for higher-order modes, a Statistical Energy Analysis (SEA), developed by *Lyon et al.*[13], is usually employed. SEA offers estimates of vibration in complex structures subjected to random loading at high frequencies providing upper-bound and general estimates of vibration response and transmission with relatively few calculations, relying on basic structural properties. Nonetheless, both SEA and classical methods face limitations due to the lack of precise information on structural damping, including material and frictional effects [11].

3.1.3 Extrapolation Methods

Extrapolation or *empirical methods* use experimental data from a reference vehicle to predict the vibration characteristics of a new vehicle. Currently, extrapolation methods are predominantly used to predict vibration motion rather than vibration stress [3]. As a result, these methods are mainly employed to establish vibration requirements for equipment rather than to evaluate the vehicle's structural integrity [11]. Extrapolation methods can be further classified into two categories:

- *Frequency Response Methods* use measurements from a reference vehicle to determine the ratio of the resulting vibration to the magnitude of the primary excitation source, as a function of frequency or bandwidth. In these methods, the fundamental source of excitation is either acoustic noise, aerodynamic noise, or both. Examples of these methods are the *Mahaffey and Smith Method*; the *Brust-tlimelblau Method*; the *Eldred, Roberts, and White Method No.1*; the *Eldred, Roberts, and White Method No.2*; the *Curtis Method*; the *Franken Method*; and the *Winter Method No.1* [3].

- *Scaling Methods* involve extrapolating specific vibration data from a reference vehicle with similar structural and configuration characteristics to predict vibration levels in a new vehicle. Notable scaling methods include the *Condos and Butler Method*, the *Barrett Method*, and the *Winter Method No.2* [3].

.

3.2 Acoustic Noise Requirements

Acoustic noise requirements ensure that structural components are designed with sufficient margins to withstand the launch environment. Therefore, the spacecraft's structure plays a crucial role in protecting its components: it must securely mount and connect all components, effectively transferring loads without failure or exposing them to potentially damaging stresses.

The acoustic vibration is typically weakest at the launch vehicle attachment plane and intensifies along the vertical axis. Hence, it is necessary to minimize the transmission of acoustic vibration along the payload axis. Acoustic energy is transmitted to the payload in two ways [4]:

- the *fluctuating pressures within the payload fairing*: these loads directly impact the exposed surfaces of the spacecraft, causing vibrations in components with a large area-to-mass ratio such as high-gain antennas and solar panels;

- the *external fluctuating pressure field*: these loads instead induces an oscillatory response in the rocket structure, which is subsequently transmitted through the spacecraft attachment ring as random vibration.

Acoustic noise excitation can induce failure modes similar to those caused by other forms of vibratory structural fatigue [4]. These failures include large displacements and rotations, causing excessive distortions, contact between components or nucleating and propagating existing cracks. Additionally, acoustic excitation can result in broken solder joints, cracked circuit boards, and damaged waveguides. Relays and pressure switches, that rely on the movement of

structural parts, are particularly vulnerable to these types of failures [4].

Ensuring that spacecraft meet acoustic requirements through rigorous testing is of paramount importance in the design and development process. By simulating and testing against expected acoustic conditions, potential vulnerabilities can be identified, and necessary design modifications can be implemented to safeguard against acoustic-induced damage. Thus, acoustic testing is a critical step in guaranteeing the reliability and success of space missions. A structural or environmental test can be classified as a *qualification test*, a *protoqualification* or *protoflight test*, or an *acceptance test*.

3.2.1   Qualification Test

A qualification test (often referred to as a *qual* test) is performed on dedicated hardware that is not intended to fly, with the objective of establishing confidence in the design. The qualification hardware is built with the same specifications and using the same manufacturing processes as the actual flight hardware. However, it is tested under more extreme conditions than the flight equipment.

A successful qualification random vibration test establishes a *qualification margin*, the difference between the qual environment and the Maximum Predicted Environment (MPE) for the mission [12]. The MPE is an envelope of the highest expected random vibration levels during the applicable event, such as launch, in a *95/50 environment*, and is either 4.9 dB or 5.0 dB above the measured data from a single flight[14]. Instead, the level of the extreme expected environment is that not exceeded on at least 99 percent of flights, estimated with 90% confidence (P99/90 level) [1].

For qualification random vibration testing, the military standard, SMC-S-016, calls for levels that are 6 dB higher than MPE and a test duration up to three minutes per axis. The NASA standard, per NASA-STD-7001A , is 3 dB higher than MPE, two minutes per axis [1].

3.2.2 Acceptance Test

An acceptance test is conducted on flight hardware typically under conditions corresponding to the MPE. If the design has already been qualified through successful qualification testing, the purpose of acceptance testing is to confirm process control, including workmanship [12]. Figure 3.4 shows the MPE curve (black) and the envelope of measured data (blue) in function of frequency and ASD. Military and NASA standards generally require one minute of random vibration testing per axis for acceptance [1].
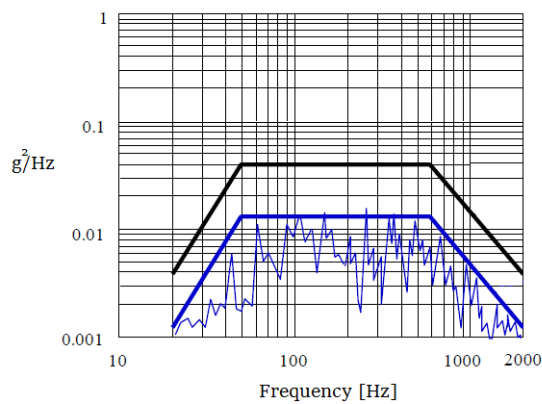
Figure 3.4: Maximum Predicted Environment Derived from an Envelope of Data from a Single Launch [14].

3.2.3 Protoqualification and Protoflight Test

A protoqualification (or *protoqual*) test and a protoflight test are often chosen instead of separate qualification and acceptance tests, when production volume is low, and building and testing dedicated hardware is not cost-effective. It's a common method for one-of-a-kind spacecraft that are launched without a flight crew. In this approach, the first-built vehicle undergoes protoqualification or protoflight testing at higher levels and for longer durations compared to later builds, which are only tested for acceptance at MPE levels. The protoqual or protoflight approach may not be acceptable to stakeholders for missions because there is no reliable method to determine if the flight hardware retains sufficient fatigue life after testing to successfully complete the mission [12].

3.3 Acoustic Test

Given the acoustic noise at lift-off and aerodynamic noise during transonic and supersonic phases are significant contributors to structural vibrations, it was a logical progression to adopt acoustic noise as a laboratory source for simulating space-vehicle vibrations [9]. The Titan program was the first to utilize acoustic testing for the design development of vehicle structures subjected to acoustic noise. Acoustic tests are essential for validating the design and mitigating risks associated with acoustic loads encountered during launch. The primary objectives of the acoustic tests are to:

- Assess the spacecraft structure's ability to withstand high acoustic pressure levels.

- Identify potential structural weaknesses or resonances.

- Validate the overall design and structural integrity to ensure mission success.

Qualification and acceptance tests for acoustic are based upon statistically expected spectral levels. The reference spectrum to be cosidered depends on the rocket that will lift the spacecraft into space. Figure 3.5 shows a typical acoustic requirement of a rocket.
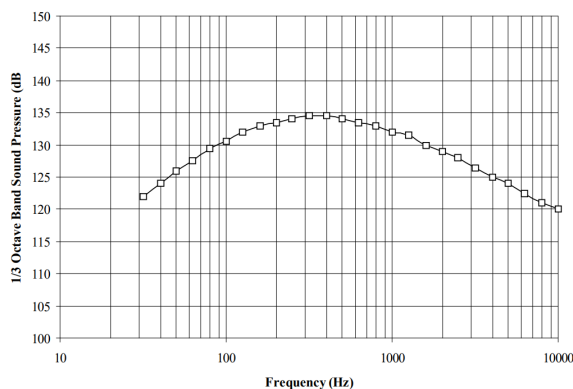
Figure 3.5: Example of acoustic noise requirement [4].

For a time-varying environment, the acoustic spectrum used for test purposes is the envelope of the spectra for each of a series of l-second time segments

overlapped by at least 50 percent. Longer time segments may be used only if it is shown that significant smoothing of the time-dependent characteristics of the spectra does not occur [1]. The associated duration is the fatigue equivalent duration in flight.
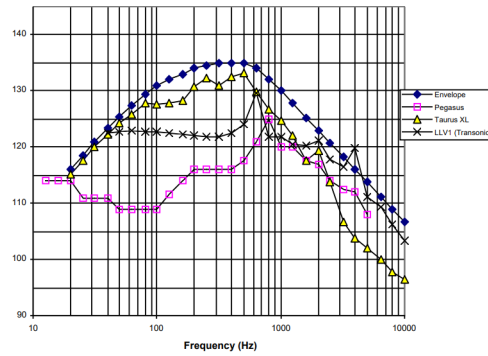
Figure 3.6: Envelope of acoustic data flight compared to data of various rockets [4].

For a time-varying flight acoustic, the fatigue equivalent duration is the time duration, at the maximum environment achieved during that flight, that would produce the same fatigue damage potential [1]. For a given flight trajectory, the equivalent duration can be assumed to be independent of the maximum environment achieved during any particular flight. The fatigue damage potential's is taken to be proportional to the fourth power of amplitude [1].

Reverberant Acoustic Chamber

The test is conducted in a reverberant acoustic chamber, designed to create a highly diffuse and uniform sound field generated by modulators connected to different horns placed in a chamber filled with nitrogen gas. Large speakers or acoustic drivers replicate the noise levels produced by rocket engines, using high-power noise generators and amplifiers to achieve the desired SPLs. Consistent sound pressure levels throughout the chamber is ensured and the noise in the room is shaped to mimic the spectrum, which the spacecraft would experience during launch inside of the shroud.

The spacecraft is equipped with an array of sensors, including accelerometers, microphones, and strain gauges. These sensors are strategically placed to monitor vibrations, acoustic pressure, and structural responses at critical points on

Figure 3.7: Reverberant Acoustic Chamber [15].

the spacecraft. Real-time data collection from sensors allows for the continuous monitoring of the spacecraft's response during the test. The duration of the test generally lasts several minutes, sufficient to replicate the acoustic environment during launch. Test procedures are governed by standards such as NASA-STD-7001 and ECSS-E-ST-32-10C, which provide guidelines for conducting these tests and ensuring spacecraft readiness for launch [16].

The Reverberant Chamber Test is a pivotal component in verifying the durability and reliability of spacecraft under the severe acoustic conditions experienced during launch. These facilities provide a very reliable means for testing, but there are very few of these, and they are very expensive to build [15]. For these reasons, new alternative ways of completing acoustic tests using a different excitation method were found.

An alternative to the reverberant room approach is the DFAN which use speakers that surround an object and subject it directly with noise. It comprises several loudspeaker arrays in a circle around the satellite, connected to a high-power amplifier to generate the required acoustic field. A set of microphones arranged around the satellite detects the acoustic pressure and uses sophisti-
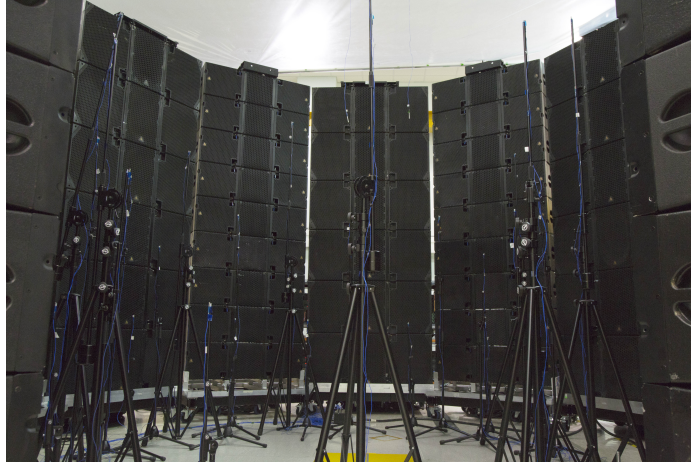
Figure 3.8: *Direct Field Acoustic Noise*, DFAN [15].

cated control software to make any required corrections [15]. Currently, there are no European standards for this type of acoustic testing. The direct acoustic field test method produces results that are considered consistent with those generated by the traditional technique.

Random Vibration Test

Although not purely an acoustic test, this test is related as it simulates the random vibrations caused by the acoustic environment during launch. For small payloads, random vibration testing is typically favored over acoustic noise testing [4]. This test consist of applying broadband, shaped, random vibration in each of three mutually perpendicular axes (preferably the principal axes) of the test item through its service attachments with a *shaker* [12]. The *Random vibration testing* has two principal objectives:

- To verify the test item design's capability, with some margin;

- To withstand the launch vibroacoustic environment;

- To screen the workmanship integrity of the flight equipment.

The frequency band span from approximately 20Hz to 2000Hz [1]. The duration of the random vibration application in each axis should be not less than

the flight duration for which the vibroacoustic environment is within 6dB of its maximum or 30 seconds [1].

Sine Vibration Test

Sine Vibration (SV) Testing involves subjecting the test article to a swept sine input over a frequency range (typically 5-100 Hz) to replicate the low-frequency launch environment [17]. Unlike the Random Vibration test, which simulates the complex vibratory environment of launch, the SV test is employed to simulate sustained sine and transient events. The spacecraft is subjected to a controlled sinusoidal input at discrete frequencies, most often as a logarithmic function of time, through a electrodynamic or hydraulic shaker. The sweep can be conducted in both upward and downward frequency directions to capture the full response of the structure. The SV levels are derived from measured flight data or based on interface acceleration levels from Coupled Loads Analysis (CLA).

The SV method is used for various purposes on a structural model but mainly on flight articles, helping identify resonant frequencies, and assesses the structural response.
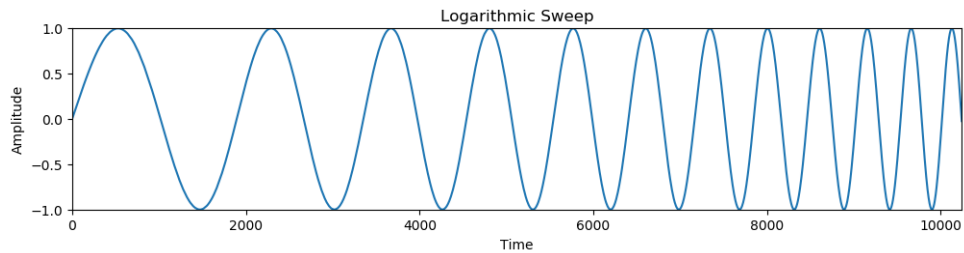
Figure 3.9: Logarithmic Sweep Rate.

SV testing is required by NASA-STD-7002 and most launch vehicle organizations as a final dynamic qualification of the payload to demonstrate acceptability for flight. NASA requirements differ however between the SV testing requirements provided in Air Force Standard SMC-S-016, Test Requirements for Launch, Upper-Stage and Space Vehicles, and the European Space Agency (ESA) Space Engineering Testing Standard ECSS-E-ST-10-03C.

27

Chapter 4

Sandwich Panels

In the challenging realm of space exploration, the need for lightweight, strong, and durable materials is crucial. Sandwich panels offer a novel and innovative solution. This chapter explores how these panels provide structural efficiency making them indispensable for spacecraft and satellite design.

4.1 Theory

In many industrial applications, such as aerospace and automotive, reducing the weight of a structure and preserving its mechanical integrity is considered as one of the most important design criterion.
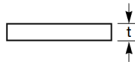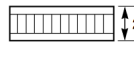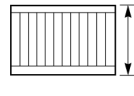
	Solid Metal Sheet	Sandwich Construction	Thicker Sandwich
Relative Stiffness	100	700 7 times more rigid	3700 37 times more rigid!
Relative Strength	100	350 3.5 times as strong	925 9.25 times as strong!
Relative Weight	100	103 3% increase in weight	106 6% increase in weight

Figure 4.1: Comparison between different structures [2].

The application of sandwich panels has become relevant due to the structure capability to maintain its strength and stiffness while being light-weight, in contrast to a solid metal sheet as shown in Figure 4.1. Thus, they are widely

used to build large parts of aircraft, spacecraft, ship, and automotive vehicle structures.

The conventional sandwich panel is made of a thick and collapsible *core* of low-density material and thin and stiff top and bottom *face sheets*. The faces could be made of composite multi-layered material, while the core is typically honeycomb, corrugated, or cellular (foam or polymeric materials). Adhesive material is used in sandwich structures to securely bond the facesheets to the core and ensure efficient load transfer between the facesheets through the core. As opposed to mechanical fasteners, adhesive offers the advantages of lower weight and reduced cost [18].
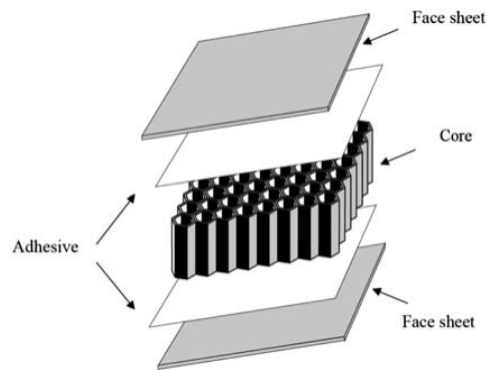
Figure 4.2: Sandwich Construction [2].

A sandwich structure follows the same logic as an I-beam [19]: the face sheets, which are away from the neutral axes, ensure axial and bending stiffness as the flanges of an I-beam; while the core, which is near the neutral axes, ensures transverse shear stiffness as the web. The core must be stiff enough to maintain the same distance between the faces and prevent the faces from sliding when a load is applied.

The design parameters that are relevant constraints in structure manufacturing are the materials of core and skins, the thickness of cores and skins, the topology of the cores, the relative thickness and the availability of volumes. The thickness of the core plays a crucial role in determining the properties of

sandwich structures. Increasing the core thickness enhances the stiffness and flexural strength of the sandwich structures [18].

There are many and disparate materials that are used in sandwich construction but in recent times new ones have been introduced. The choice of face sheet and core materials depends heavily on the intended operational environment. In space industry sandwich panel face sheets are commonly fabricated using aluminium or graphite/epoxy composite panels while the core is typically fabricated using a honeycomb or foam construction [18].

4.2 Core materials

4.2.1 Honeycomb Materials

Honeycomb sandwich panels are commonly used in aviation and aerospace applications because of their simple production and higher efficiency in stiffness and shear strength. Furthermore, honeycomb core sandwich structures exhibit enhanced shock wave absorption, crash-worthiness, and low-velocity impact resistance [20].

Different cell shapes such as hexagonal, OX, flex core are available [21]. Among these, standard hexagonal honeycomb structure is the most common cellular honeycomb. The hexagonal honeycomb is widely used because of its simple manufacture, low cost, and high structural efficiency. The honeycomb core materials can be metallic such as aluminium or non-metallic materials such as fibre reinforced plastics from carbon, aramid, fibre glass. Honeycomb materials of titanium, stainless steel and other types are not frequently used in aerospace applications. The mechanical properties of honeycomb core materials are significantly influenced by the characteristics of the materials from which they are manufactured, as well as the geometry of the honeycomb, so is significantly important to select the right configuration.

Aluminium Honeycomb

Aluminium honeycomb structures are known for their high specific stiffness, energy absorption, efficient heat transfer, and electromagnetic shielding properties [22]. They offer excellent performance relative to their cost. Al-5056

and Al-5052 are usually employed in aerospace.

Young's Modulus E	Poisson's Ratio ν	Density ρ
70 GPa	0.3	2700 kg/m^3

Table 4.1: Mechanical properties of aluminium.

The table above presents the mechanical properties of aluminium. When discussing the mechanical properties of an aluminum honeycomb structure, it is important to consider not only the type of aluminum alloy used but also the parameters that define the hexagonal cells, as both influence the overall properties of the honeycomb.

Aramid Fiber Paper Honeycomb

There are three types of aramid fibre reinforced honeycomb. A popular type of fibre-impregnated honeycomb uses NOMEX® paper coated with phenolic or other resins. It exhibits good performance, such as high specific strength, excellent flame retardancy, good corrosion resistance, and shock absorption [23]. NOMEX® can be considered a good shield candidate material for radio-protection [24]. Its mechanical properties as a core are lower than aluminium, especially in terms of modulus.

HexWeb® HRH-10 is widely recognized in the aerospace industry as a highly durable and environmentally resistant core material used in sandwich panels for radomes, fairings, helicopter blades, and flaps [25].

| HexWeb® HRH-10 | Compression | | | Plate Shear | | | |
| | Bare | Stabilised | | L Direction | | W Direction | |
	Strength (MPa)	Strength (MPa)	Modulus (MPa)	Strength (MPa)	Modulus (MPa)	Strength (MPa)	Modulus (MPa)
HRH-10-3.2-29	0.64	0.79	55	0.62	26	0.34	10
HRH-10-3.2-123	10.60	11.00	500	3.10	105	1.90	53
HRH-10-4.8-64	3.45	3.72	193	1.69	54	0.97	32
HRH-10-6.4-24	0.55	0.62	41	0.48	21	0.34	9

Table 4.2: HRH-10 Honeycomb Properties [21].

KEVLAR® honeycomb exhibits superior mechanical and thermal properties compared to NOMEX® honeycomb [26]. Kevlar 49 fabric, impregnated with epoxy resin, is often chosen for applications requiring low dielectric properties to allow RF signal transmission, such as in antenna reflectors [27]. These honeycombs offer excellent thermal stability and a lower coefficient of thermal

expansion, but their production costs are higher due to manufacturing complexities [28].

| Material | Compressive | | Plate Shear | | | |
| | Stabilised | | L Direction | | W Direction | |
	Strength (MPa)	Modulus (GPa)	Strength (MPa)	Modulus (GPa)	Strength (MPa)	Modulus (GPa)
HRH-49 − 1/4 − 2.1	896.2	689.5	172.4	585.0	344.8	18.6

Table 4.3: Kevlar Honeycomb Properties [21].

KOREX is a newly available honeycomb made from KOREX aramid-fibre paper. It provides improved strength-to-weight ratios and/or lower moisture absorption compared to traditional Nomex honeycombs of similar configurations [21].

| Material | Compressive Strength | | Plate Shear | | | |
| | Bare (MPa) | Stabilized (MPa) | L Direction | | W Direction | |
			Strength (MPa)	Modulus (MPa)	Strength (MPa)	Modulus (MPa)
KOREX − 1/8 − 3.0	1.79	1.93	1.23	99.7	0.72	48.3
KOREX − 1/8 − 4.5	3.66	4.07	2.48	203.2	1.52	82.7
KOREX − 1/8 − 6.0	6.76	6.89	3.58	238.0	2.14	110.1
KOREX − 5/32 − 2.4	1.59	1.79	1.16	80.8	0.70	45.6
KOREX − 3/16 − 2.0	1.03	1.10	0.59	82.7	0.48	34.5
KOREX − 3/16 − 3.0	1.93	2.14	1.52	137.9	0.79	62.7
KOREX − 3/16 − 4.5	4.01	4.55	2.55	213.4	1.52	77.3
KOREX − 1/4 − 1.5	0.69	0.76	0.59	51.4	0.32	21.4
KOREX − 3/8 − 4.5	3.58	3.86	2.37	152.5	1.30	57.4
KOREX − 3/80X − 1.5	0.62	0.69	0.45	29.0	0.34	29.0

Table 4.4: KOREX Honeycomb Properties [21].

4.2.2 Foam

Foams have been widely employed as structural cores. Higher damping properties, ease of manufacturing, shaping, and bonding are some of the advantages of cellular foams, but the stiffness-to-weight ratios tend to be lower than honeycomb structures. Commonly used foams in spacecraft applications include Polymethacrylimide (PMI) foams, PVC foams, silicon carbide (SiC) foams, and metal foams.

PMI foams were successfully introduced in 1971 as structural sandwich core for helicopter fuselage panels. PMI has been used as a substitute for honeycomb cores in applications where lateral forces, moisture absorption, and corrosion

are critical concerns [29]. While honeycombs provide a superior strength-to-weight ratio, PMI rigid foam cores present a viable alternative when cost-effective co-curing is utilized and a slight increase in weight is acceptable [29]. PMI offer excellent mechanical properties among polymer cellular foams and are known for their high temperature resistance. *Rohacell* structural sandwich cores is state-of-the-art technology for the manufacturing of helicopter rotor blades.

Material	Young's Modulus (MPa)	Poisson's Ratio	Density (kg/m^3)
Rohacell32	23	0.2	32
Rohacell51	36	0.3	55
Rohacell71	72	0.25	75
Rohacell110	119	0.28	110
Rohacell200	263	0.17	205

Table 4.5: Mechanical Properties of Rohacell.

PVC foams are employed in various aerospace sandwich structures. Cross-linked types offer greater rigidity and a higher stiffness-to-weight ratio, while linear types are more ductile and soften at elevated temperatures [30]. PVC is less expensive than PMI, but its temperature resistance is typically limited to around 80°C (compared to the 225°C of PMI [29]), making it unsuitable as a core material for certain aerospace designs.

Young's Modulus E (GPa)	Poisson's Ratio ν	Density ρ (kg/m^3)
2.5-4.0	0.40-0.45	1380-1450

Table 4.6: Properties of PVC Foam.

Silicon Carbide foams are porous, open-celled structures made from ceramic ligaments. They are lightweight, strong, resistant to thermal shock, and exhibit both electrical and thermal conductivity. SiC foams can withstand remarkably high temperatures, up to 2200°C, making them suitable for applications such as heat exchangers, heat shielding, and space mirrors [31].

Metal foams are commonly used for energy absorption in lightweight structural

applications [32]. They have low densities and exhibit good shear and fracture strength. Open-cell foams offer large accessible surface areas and high cell-wall conductivity, providing excellent heat transfer abilities. Additionally, metallic foams possess acoustic properties that make them suitable for environments requiring sound absorption.

4.3 Face Sheets materials

In aerospace applications, prepregs, composed of unidirectional fibres, are commonly used for face sheets due to their specific stiffness, low coefficient of thermal expansion, and space-proven reliability. Initially, aluminium was widely used until the introduction of composite materials. Today, fibre-reinforced composite materials are predominantly used for sandwich panel faces in most missions. These materials offer enhanced mechanical properties that can be tailored by adjusting fibre orientation and the number of plies to achieve greater stiffness and strength.

Glass Fibre-Reinforced Plastic

GRFP honeycombs are known for their high specific strength and stiffness, electrical properties, and moisture, heat, and chemical resistance [33]. They are commonly used in antennae [34][35] and heat shielding in re-entry vehicles like Gemini and Apollo.

Material	E_1 (GPa)	E_2 (GPa)	E_3 (GPa)	$G_{13} = G_{12}$ (GPa)	$G_2 3$ (GPa)	Poisson's Ratio ν	Density ρ (kg/m³)
1	4.669	4.351	4.351	3.250	1.625	0.17	1900
2	4.408	4.081	4.081	1.100	0.550	0.17	1900
3	5.639	4.926	4.926	0.750	0.375	0.17	1900

Table 4.7: Equivalent properties of GRFP [36].

Carbon Fibre-Reinforced Plastic

Carbon Fiber-Reinforced Plastics (CFRP) is frequently chosen as face sheets in satellite sandwich structures to enhance weight efficiency and it is often coupled with an aluminium honeycomb core.

Material	E_1 (GPa)	E_2 (GPa)	E_3 (GPa)	$G_{13} = G_{12}$ (GPa)	G_23 (GPa)	Poisson's Ratio ν	Density ρ (kg/m^3)
1	6.695	6.314	6.314	2.700	1.350	0.3	1388
2	6.469	5.626	5.626	2.050	1.025	0.3	1388
3	12.34	12.34	10.45	6.450	3.225	0.3	1388

Table 4.8: Equivalent properties of CFRP [36].

4.4 Analytical Theory for Effective Material Properties of Honeycomb Sandwich Plates

Sandwich structures are commonly analyzed using the FEM, which provides robust modeling capabilities. The outer skins of these structures are relatively straightforward to model, relying on well-established *laminate theory*. However, the mechanical modeling of the core, especially for honeycomb configurations, presents more complexity. To overcome this, homogenization techniques are employed to substitute the heterogeneous honeycomb core with a simplified, continuous solid layer possessing *effective* material properties. This approach circumvents the challenges posed by the inherent structural heterogeneities within the honeycomb core [37].
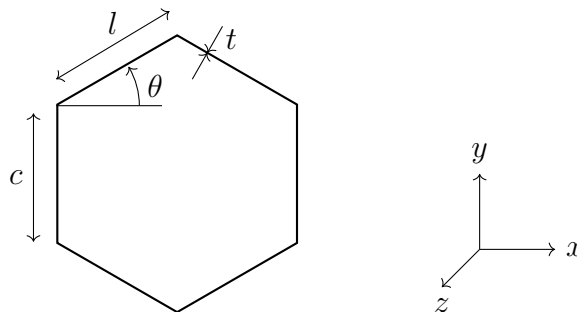
Figure 4.3: Configuration of a Unit Cell.

The derivation of effective material properties for honeycomb structures typically involves analyzing a unit cell, a representative repeating element within the honeycomb lattice. This unit-cell analysis allows for the estimation of equivalent and homogenized mechanical properties.

The closed-form expressions developed by Gibson and Ashby (1999) are widely used in the literature to estimate the effective elastic moduli of regular honeycomb cores, particularly in the context of free-vibration analysis of sandwich panels. Gibson and Ashby's method remains the most relevant framework

35

for determining these effective material properties. Their approach assumes a linear-elastic response in the honeycomb structure, deriving core properties by considering the bending behavior of the cell walls. The following equations describe the effective moduli for a uniformly isotropic wall material [38]:

$$E_{xx} = \left(\frac{t}{l}\right)^3 \frac{\cos(\theta)}{\sin(\theta)^2 \left(\frac{c}{l} + \sin(\theta)\right)} E_c \tag{4.1}$$

$$E_{yy} = \left(\frac{t}{l}\right)^3 \frac{\left(\frac{c}{l} + \sin(\theta)\right)}{\cos(\theta)^3} E_c \tag{4.2}$$

$$E_{zz} = \left(\frac{t}{l}\right) \frac{\left(\frac{c}{l} + 1\right)}{\cos(\theta) \left(\frac{c}{l} + \sin(\theta)\right)} E_c \tag{4.3}$$

where l and c represent the length of the sides, t is the thickness of the wall, E_c is the elastic modulus of the core material, and ν_c is the Poisson's ratio. The angles and geometric parameters, such as θ, play a crucial role in defining the anisotropic behavior of the honeycomb.

The following equations define the Poisson's ratios [38]:

$$\nu_{xy} = \frac{\cos^2(\theta)}{\left(\frac{c}{l} + \sin(\theta)\right) \sin(\theta)} \tag{4.4}$$

$$\nu_{xz} = \nu_c \frac{E_{xx}}{E_{zz}} \tag{4.5}$$

$$\nu_{yz} = \nu_c \frac{E_{yy}}{E_{zz}} \tag{4.6}$$

while the shear moduli [38]:

$$G_{xy} = \left(\frac{t}{l}\right)^3 \left(\frac{c}{l}\right)^2 \left(1 + \frac{c}{4l}\right) \frac{\cos(\theta)}{\cos(\theta)^2} E_c \tag{4.7}$$

$$G_{xz} = G_c \left(\frac{t}{l}\right) \frac{\cos(\theta)}{\frac{c}{l} + \sin(\theta)} \tag{4.8}$$

$$G_{yz} = G_c \left(\frac{t}{l}\right) \frac{\frac{c}{l} + \sin(\theta)}{\cos(\theta) \left(1 + \frac{c}{l}\right)} \tag{4.9}$$

The density of the honeycomb core is expressed by $\rho = \left(\frac{t}{l}\right) \frac{\left(1 + \frac{h}{l}\right)}{\cos(\theta)\left(\frac{h}{l} + \sin(\theta)\right)} \rho_s$ [39]. These expressions provide a comprehensive framework for calculating the effective elastic and shear moduli of honeycomb cores, assuming isotropic wall

material properties. By employing these formulas, the complexities of hetero-geneous material behavior are reduced, allowing for more efficient analysis of sandwich structures.

4.4.1 Regular Honeycomb Case

For a regular honeycomb structure, where c is equal to l and the internal angle θ is 30° [39], the previous equations can be simplified accordingly. In this specific case, the general expressions for the effective material properties are modified to reflect the symmetry and geometric constraints of a regular honeycomb configuration.

$$E_{xx} = \frac{4\sqrt{3}}{3} \left(\frac{t}{l}\right)^3 E_c \tag{4.10}$$

$$E_{yy} = \frac{4}{\sqrt{3}} \left(\frac{t}{l}\right)^3 E_c \tag{4.11}$$

$$E_{zz} = \frac{8}{3} \left(\frac{t}{l}\right) E_c \tag{4.12}$$

The above equations describe the effective Young's moduli in the x, y, and z directions. For the in-plane directions (E_{xx} and E_{yy}), the cubic dependency on the relative thickness $\frac{l}{t}$ the influence of the cell wall thickness on the stiffness. Meanwhile, E_{zz}, the out-of-plane Young's modulus, has a linear dependence on $\frac{l}{t}$, signifying a different deformation mechanism in the out-of-plane direction.

$$\nu_{xy} \approx 1 \tag{4.13}$$

$$\nu_{xz} = \nu_c \frac{\sqrt{3}}{2} \left(\frac{t}{l}\right)^2 \tag{4.14}$$

$$\nu_{yz} = \nu_c \frac{3}{2\sqrt{3}} \left(\frac{t}{l}\right)^2 \tag{4.15}$$

Here, $\nu_{xy} \approx 1$ indicates that the material exhibits nearly incompressible be-havior in the plane of the honeycomb, a typical characteristic for hexagonal structures. The Poisson's ratios ν_{xz} and ν_{yz} describe the coupling between in-plane and out-of-plane deformations, with their values scaling quadratically with $\left(\frac{t}{l}\right)$, reflecting the geometric constraints of the honeycomb. Finally, the

shear moduli are expressed as:

$$G_{xy} = \frac{5\sqrt{3}}{6} \left(\frac{t}{l}\right)^3 E_c \tag{4.16}$$

$$G_{xz} = \frac{\sqrt{3}}{3} \left(\frac{t}{l}\right) G_c \tag{4.17}$$

$$G_{yz} = \frac{3}{2\sqrt{3}} \left(\frac{t}{l}\right) G_c \tag{4.18}$$

These equations show how the shear moduli depend on both the relative thickness of the cell walls and the stiffness of the material. Similar to the Young's moduli, the in-plane shear modulus G_{xy} follows a cubic relationship, while the out-of-plane components G_{xz} and G_{yz} scale linearly with $\left(\frac{t}{l}\right)$.

Chapter 5

High Order Plate Finite Element Models

In this chapter, the numerical model adopted base on finite element procedure is presented. The governing equation for the static, modal and dynamical problem are carried out by the PVD. High-order 2D plate models are implemented by means of the CUF. In this framework, both ESL models and LW models are taken into account, in a unified framwork based on a recusive index notation. The stiffness and mass matrices, and the external force vector are written in terms of Fundamental Nuclei (FN), the basic building blocks of the present models, invariant to the kinematic models and theory of structure approximation adopted.

5.1 Governing Equations

5.1.1 Geometrical Relations

Under the hypothesis of small displacements and rotations, the strain tensor components are related to the displacement components by the geometrical relations through linear differential relations. If $u = \{u \ v \ w\}^T$ is the vector of

the displacements:

$$\varepsilon_{xx} = \frac{\partial u}{\partial x}, \quad \varepsilon_{yy} = \frac{\partial v}{\partial y}, \quad \varepsilon_{zz} = \frac{\partial w}{\partial z}$$

$$\gamma_{xy} = \frac{1}{2}\left(\frac{\partial u}{\partial y} + \frac{\partial v}{\partial x}\right), \quad \gamma_{yz} = \frac{1}{2}\left(\frac{\partial v}{\partial z} + \frac{\partial w}{\partial y}\right), \quad \gamma_{zx} = \frac{1}{2}\left(\frac{\partial w}{\partial x} + \frac{\partial u}{\partial z}\right)$$

$$(5.1)$$

By using the formal matrix of derivatived operators $\mathbf{b}$:

$$\boldsymbol{\varepsilon} = \mathbf{b}\mathbf{U} \rightarrow \begin{bmatrix} \varepsilon_{xx} \\ \varepsilon_{yy} \\ \varepsilon_{zz} \\ \varepsilon_{xx} \\ \varepsilon_{yz} \\ \varepsilon_{xy} \end{bmatrix} = \begin{bmatrix} \frac{\partial}{\partial x} & 0 & 0 \\ 0 & \frac{\partial}{\partial y} & 0 \\ 0 & 0 & \frac{\partial}{\partial z} \\ \frac{\partial}{\partial z} & 0 & \frac{\partial}{\partial x} \\ 0 & \frac{\partial}{\partial z} & \frac{\partial}{\partial y} \\ \frac{\partial}{\partial y} & \frac{\partial}{\partial x} & 0 \end{bmatrix} \begin{bmatrix} u_x \\ u_y \\ u_z \end{bmatrix} \qquad (5.2)$$

5.1.2 Constitutive equation

In the context of high order plate finite element models, the accurate rappresentation of the properties and the behavior of the material is crucial. To this end, the strain tensor and the stress tensor are defined.

The strain tensor $\boldsymbol{\varepsilon}$ in three dimensions can be represented as:

$$\boldsymbol{\varepsilon} = \begin{bmatrix} \varepsilon_{xx} & \varepsilon_{xy} & \varepsilon_{xz} \\ \varepsilon_{yx} & \varepsilon_{yy} & \varepsilon_{yz} \\ \varepsilon_{zx} & \varepsilon_{zy} & \varepsilon_{zz} \end{bmatrix} \qquad (5.3)$$

Similarly, the stress tensor $\boldsymbol{\sigma}$ can be expressed in a matrix form:

$$\boldsymbol{\sigma} = \begin{bmatrix} \sigma_{xx} & \tau_{xy} & \tau_{xz} \\ \tau_{yx} & \sigma_{yy} & \tau_{yz} \\ \tau_{zx} & \tau_{zy} & \sigma_{zz} \end{bmatrix} \qquad (5.4)$$

Due to Cauchy's Theorem, the two matrices will be real and symmetrical ($\varepsilon_{ij} = \varepsilon_{ji}$, $\tau_{ij} = \tau_{ji}$). Only six components represent every tensor. These

components can be written in a vector form by using the Voigt notation:

$$\boldsymbol{\varepsilon} = \left\{ \varepsilon_{xx} \quad \varepsilon_{yy} \quad \varepsilon_{zz} \quad \varepsilon_{yz} \quad \varepsilon_{xz} \quad \varepsilon_{xy} \right\}^T = \left\{ \varepsilon_{xx} \quad \varepsilon_{yy} \quad \varepsilon_{zz} \quad 2\gamma_{yz} \quad 2\gamma_{xz} \quad 2\gamma_{xy} \right\}^T \tag{5.5}$$

$$\boldsymbol{\sigma} = \left\{ \sigma_{xx} \quad \sigma_{yy} \quad \sigma_{zz} \quad \tau_{yz} \quad \tau_{xz} \quad \tau_{xy} \right\}^T \tag{5.6}$$

Under the hypothesis of linear elasticity, it is possible to write a governing relation for the stress tensor in a resulting additional equation relating the stress tensor to the strain tensors previously defined through the material stiffness matrix $\mathbb{C}$. In linear elasticity, the constitutive law is expressed by the Hooke's law:

$$\boldsymbol{\sigma} = \mathbb{C}\boldsymbol{\varepsilon} \tag{5.7}$$

Here, $\mathbb{C}$ is a 6×6 matrix that encapsulates the material properties, including Young's modulus, Poisson's ratio, and shear modulus.

5.1.3 Pure Displacement Formulation

The governing equations are carried out by means of the the PVD. This approach lead to the integral form of the governing equation, in which it is possible to implement a finite element procedure. In the following, a pure displacement formulation will be adopted, namely the only unknowns of the governing equations are displacement components. The PVD states that the virtual variation of the total internal work, written as the difference between the internal and external work, is null:

$$\delta\mathcal{L} = \delta\mathcal{L}_{\text{int}} - \delta\mathcal{L}_{\text{ext}} = 0 \tag{5.8}$$

Here, $\delta\mathcal{L}_{\text{int}}$ represents the virtual internal work, and $\delta\mathcal{L}_{\text{ext}}$ represents the virtual external work.

Virtual Internal Work

The virtual internal work is the potential energy stored during the deformation process. The expression of the virtual internal work can assume the form:

$$\delta\mathcal{L}_{\text{int}} = \int_V \delta\boldsymbol{\varepsilon}^T \boldsymbol{\sigma}\, dV \tag{5.9}$$

where $\delta\boldsymbol{\varepsilon}$ is the virtual strain and $\boldsymbol{\sigma}$ is the stress.

Virtual External Work

The virtual external work is the work done by external forces $\mathbf{f}$ on the real displacement field:

$$\delta\mathcal{L}_{\text{ext}} = \int_V \delta\mathbf{u}^T \mathbf{f}\, dV \tag{5.10}$$

By incorporating the constitutive equation and the geometrical relation:

$$\delta\boldsymbol{\varepsilon} = \mathbf{b}\delta\mathbf{u} \quad \Rightarrow \quad \delta\boldsymbol{\varepsilon}^T = \delta\mathbf{u}^T \mathbf{b}^T, \quad \boldsymbol{\sigma} = \mathbb{C}\boldsymbol{\varepsilon} = \mathbb{C}\mathbf{b}\mathbf{u} \tag{5.11}$$

Eq. 5.10 can be rewritten as follow:

$$\int_V \delta\mathbf{u}^T \mathbf{b}^T \mathbb{C}\mathbf{b}\mathbf{u}\, dV = \int_V \delta\mathbf{u}^T \mathbf{f}\, dV \tag{5.12}$$

5.2 CUF's Fundamental Nuclei

Classical Plate Theory (CPT) and First-Order Shear Deformation Theory (FSDT) have been widely used for the analysis of thin plates. However, these theories are based on assumptions that limit their applicability:

- CPT assumes that normals to the mid-surface remain straight and normal after deformation, neglecting shear deformation. This is adequate for thin plates but not for thick or laminated structures.

- FSDT includes shear deformation but assumes a constant shear strain across the thickness, which can lead to inaccuracies, especially in thick laminates or sandwich structures.

These limitations necessitate the development of high-order theories that can more accurately describe the behavior of composite and sandwich panels, especially under complex loading conditions. These conventional theories fail to accurately capture the displacement and transverse stress fields that are piecewise continuous through the thickness, a characteristic of multi-layered structures. To address these challenges, it is essential that both displacements and transverse stresses be C^0 continuous functions in the thickness direction z. This requirement is commonly referred to as the C^0 continuity condition.

Zig-Zag theories (ZZ) introduce a more realistic approximation by allowing the in-plane displacements to vary linearly within each layer, with sudden changes in slope at the interfaces between layers. This zig-zag pattern effectively models the piecewise linear behavior of the displacement field and improve the representation of these stresses by ensuring continuity at the interfaces between layers, which is crucial for predicting failure modes such as delamination.

The CUF offers a versatile and systematic framework for developing high-order models. CUF is based on the idea of expanding the displacement field in the thickness direction using a set of hierarchical functions, such as polynomials or trigonometric functions. If a plate model, with thickness defined along the z-axis and the mid-surface lying in the $x-y$ reference plane, is considered, the general form of the three-dimensional displacement field is given by:

$$\mathbf{u}(x,y,z) = F_\tau(z)\mathbf{u}_\tau(x,y) \quad \tau = 1, 2, \ldots, M \quad (5.13)$$

where $F_\tau(z)$ are the thickness expansion functions used to expand the displacement field through the thickness of the plate, M is the order of expansion, and $\mathbf{u}_\tau$ is the continuous mid-surface displacement field. The displacement components, at any height z through the thickness, are influenced by the properties of the reference surface of the plate, due to the expansion expressed through

43

the set of functions $F_\tau(z)$, and can be explicited as:

$$
\begin{cases}
u_x(x,y,z) = F_1(z)u_{x_1}(x,y) + F_2(z)u_{x_2}(x,y) + \cdots + F_M(z)u_{x_M}(x,y) \\
u_y(x,y,z) = F_1(z)u_{y_1}(x,y) + F_2(z)u_{y_2}(x,y) + \cdots + F_M(z)u_{y_M}(x,y) \\
u_z(x,y,z) = F_1(z)u_{z_1}(x,y) + F_2(z)u_{z_2}(x,y) + \cdots + F_M(z)u_{z_M}(x,y)
\end{cases}
$$
$$(5.14)$$

The mid-surface displacement field is further discretized by classical FE approach, using the set of 2D shape functions to approximate the continous field in terms of nodal components $\mathbf{u}_{\tau_i}$.

$$
\mathbf{u}_\tau(x,y) = N_i(x,y)\mathbf{u}_{\tau_i} \quad i = 1, 2, \ldots, N_n \tag{5.15}
$$

where N_n represents the number of terms used in the discretization process and $N_i(x,y)$ is the set of classical 2D Lagrange polynomials.

In the context of finite element implementation, the energy contributions within the chosen variational principle necessitate defining virtual quantities, such as displacement and strain fields. In this regard, the virtual motion field is approximated using the same formalism as that employed for the actual field, but with an index expansion that is independent of the one used for the real field:

$$
\delta\mathbf{u}(x,y,z) = F_s(z)\delta\mathbf{u}_s(x,y) = F_s(z)N_j(x,y)\delta\mathbf{u}_{sj} \quad j = 1, 2, \ldots, N_n \tag{5.16}
$$

Substituing the real and virtual displacement relations in Eq. 5.12:

$$
\int_V F_s(z)\delta\mathbf{u}_s(x,y)^T \mathbf{b}^T \mathbb{C}\mathbf{b}F_\tau(z)\mathbf{u}_\tau(x,y)\,dV = \int_V F_s(z)\delta\mathbf{u}_s(x,y)^T \mathbf{f}\,dV \tag{5.17}
$$

$$
\int_V \delta\mathbf{u}_{sj}^T F_s N_j \mathbf{b}^T \mathbb{C}\mathbf{b}F_\tau N_i \mathbf{u}_{\tau i}\,dV = \int_V \delta\mathbf{u}_{sj}^T F_s N_j \mathbf{f}\,dV \tag{5.18}
$$

$$
\delta\mathbf{u}_{sj}^T \left[\int_V F_s N_j \mathbf{b}^T \mathbb{C}\mathbf{b}F_\tau N_i\,dV \right] \mathbf{u}_{\tau i} = \delta\mathbf{u}_{sj}^T \left[\int_V F_s N_j \mathbf{f}\,dV \right] \tag{5.19}
$$

$$
\left[\int_V \mathbf{B}_{sj}^T \mathbb{C}\mathbf{B}_{\tau i}\,dV \right] \mathbf{u}_{\tau i} = \int_V F_s N_j \mathbf{f}\,dV \tag{5.20}
$$

where the matrix $\mathbf{B}_{\tau i}$ is defined as:

$$\mathbf{B}_{\tau i} = \begin{bmatrix} F_\tau N_{i,x} & 0 & 0 \\ 0 & F_\tau N_{i,y} & 0 \\ 0 & 0 & F_{\tau,z} N_i \\ F_{\tau,z} N_i & 0 & F_\tau N_{i,x} \\ 0 & F_{\tau,z} N_i & F_\tau N_{i,y} \\ F_\tau N_{i,y} & F_\tau N_{i,x} & 0 \end{bmatrix} \tag{5.21}$$

The matrix $\mathbf{B}_{sj}$ is defined similarly to $\mathbf{B}_{\tau i}$, applying the derivative operators to the shape functions and CUF expansion functions of the virtual displacement field.

5.2.1 Classical 2D shape functions for mid-surface interpolation

The finite element approximation is approached with varying levels of polynomial accuracy to address different structural elements: linear Q4, parabolic Q9, and cubic Q16 finite elements are employed. The Q9 element, a higher-order quadrilateral element which will be used in the following analysis, significantly enhances the accuracy of simulations involving two-dimensional structures.

In this case, the shape functions in the natural reference frame (ξ, η) are expressed as [40]:

$$N_i = \frac{1}{4} \left(\eta^2 + \eta \eta_i \right) \left(\xi^2 + \xi \xi_i \right), \quad i = 1, 3, 5, 7, \tag{5.22}$$

$$N_i = \frac{1}{2} \xi_i^2 \left(\xi^2 + \xi \xi_i \right) \left(1 - \eta^2 \right) + \frac{1}{2} \eta_i^2 \left(\eta^2 + \eta \eta_i \right) \left(1 - \xi^2 \right), \quad i = 2, 4, 6, 8, \tag{5.23}$$

$$N_i = (1 - \eta^2)(1 - \xi^2), \quad i = 9. \tag{5.24}$$

Therefore, once the nodal displacements are computed, the displacement field of a Q9 domain in the physical reference frame is written as:

$$\begin{cases} u_x = \sum_{i=1}^{9} N_i u_{x_i} \\ u_y = \sum_{i=1}^{9} N_i u_{y_i} \end{cases} \tag{5.25}$$

The adoption of the natural coordinate system is crucial for simplifying the mathematical representation and numerical integration of stiffness matrix elements. The natural coordinate system, defined by the coordinates (ξ, η) within the domain $[-1, 1]$, allows for a consistent representation of shape functions and their derivatives across all finite elements, regardless of the FE shape and definition. This framework is particularly advantageous for employing numerical integration techniques such as Gauss-Legendre quadrature, which approximate integrals as weighted sums evaluated at specific Gauss Points. The integral computation relies solely on evaluating the integrand at these points, multiplied by constants known as *quadrature weights*, which are tabulated and depend on the number of quadrature points used.

The transformation from the Cartesian coordinate system to the natural coordinate system is then performed by the Jacobian.

5.2.2 Stiffness Matrix

The fundamental nucleus of the stiffness matrix $\mathbf{K}_{\tau sij}$ is a 3×3 matrix that depends on the indices of the discretization and the mathematical model used to describe the displacement field:

$$\mathbf{K}_{\tau sij} = \int_V F_s N_j \mathbf{b}^T \mathbb{C} \mathbf{b} F_\tau N_i \, dV = \int_V \mathbf{B}_{sj}^T \mathbb{C} \mathbf{B}_{\tau i} \, dV \qquad (5.26)$$

After defining the FN based on the element definitions in the global domain discretization, the total stiffness matrix is assembled by considering the connectivity between elements and accounting for the finite nodes and CUF expansion nodes. By summing over the recursive indices expansion i and j, τ and s, the the internal and external forces vectors, and the mass matrix for the single element considered, are obtained straightforwardly by following the CUF assembling procedure.

5.2.3 Load vector

The fundamental nucleus of the nodal load vector $\mathbf{P}_{sj}$ is a 3×1 vector representing the load vector in terms of generalized nodal forces:

$$\mathbf{P}_{sj} = \int_V F_s N_j \mathbf{f} \, dV \tag{5.27}$$

5.2.4 Mass Matrix

In dynamic structural problems, the mass matrix accounts for inertia forces. According to the Principle of Virtual Displacements:

$$\delta \mathcal{L}_{\text{int}} + \delta \mathcal{L}_{\text{ine}} = \delta \mathcal{L}_{\text{ext}} \tag{5.28}$$

Following the same procedure as for the internal and external virtual work:

$$
\begin{aligned}
\delta \mathcal{L}_{\text{ine}} &= \int_V \delta \mathbf{u}^T \rho \ddot{u} \, dV \\
&= \int_V \delta \mathbf{u}_{sj}^T F_s N_j \rho F_\tau N_i \ddot{\mathbf{u}}_{\tau i} \, dV \\
&= \delta \mathbf{u}_{sj}^T \left[\int_V F_s N_j \rho \mathbf{I} F_\tau N_i \, dV \right] \ddot{\mathbf{u}}_{\tau i}
\end{aligned}
\tag{5.29}
$$

The term in brackets represents the FN of the mass matrix, which follows the same procedure described for assembling the total mass matrix of the structure. The inertia forces only work for the corresponding component in the vector of virtual variations, requiring an identity matrix in the mass matrix since each acceleration only works with its corresponding component. For this reason, the mass matrix is always diagonal and symmetric:

$$\mathbf{M}_{\tau sij} = \begin{bmatrix} M_{11} & 0 & 0 \\ 0 & M_{22} & 0 \\ 0 & 0 & M_{33} \end{bmatrix}_{\tau sij} \tag{5.30}$$

$$\mathbf{M}_{kk} = \int_V F_s N_j \rho F_\tau N_i \, dV \quad k = 1, 2, 3 \tag{5.31}$$

5.2.5 Jacobian Matrix

During the calculation of each component of the fundamental nucleus of the stiffness or mass matrix, it is necessary to deal with the derivatives of the thickness and in-plane functions in the physical reference frame. Since shape functions N_i are defined in the natural reference frame, it is necessary to build a tool that relates the derivatives in these two different reference frames: the Jacobian.

To calculate the derivatives of the shape functions with respect to Cartesian coordinates, the derivatives using the chain rule are expressed:

$$\frac{\partial N_i}{\partial \xi} = \frac{\partial N_i}{\partial x}\frac{\partial x}{\partial \xi} + \frac{\partial N_i}{\partial y}\frac{\partial y}{\partial \xi} \tag{5.32}$$

$$\frac{\partial N_i}{\partial \eta} = \frac{\partial N_i}{\partial x}\frac{\partial x}{\partial \eta} + \frac{\partial N_i}{\partial y}\frac{\partial y}{\partial \eta} \tag{5.33}$$

These expressions can be rewritten using the Jacobian matrix as:

$$\begin{Bmatrix} \dfrac{\partial}{\partial \xi} \\ \dfrac{\partial}{\partial \eta} \end{Bmatrix} = \begin{bmatrix} \dfrac{\partial x}{\partial \xi} & \dfrac{\partial y}{\partial \xi} \\ \dfrac{\partial x}{\partial \eta} & \dfrac{\partial y}{\partial \eta} \end{bmatrix} \begin{Bmatrix} \dfrac{\partial}{\partial x} \\ \dfrac{\partial}{\partial y} \end{Bmatrix} \tag{5.34}$$

Since these derivatives are known in the natural reference frame, the Inverse Jacobian Matrix is used:

$$\begin{Bmatrix} \dfrac{\partial}{\partial x} \\ \dfrac{\partial}{\partial y} \end{Bmatrix} = J^{-1} \begin{Bmatrix} \dfrac{\partial}{\partial \xi} \\ \dfrac{\partial}{\partial \eta} \end{Bmatrix} \tag{5.35}$$

The Jacobian matrix must necessarily be non-singular, a condition ensured by the definition of a regular discretisation. Considering isoparametric elements, it is possible to approximate the geometry by the nodal coordinates:

$$\begin{cases} x = \sum_{i=1}^{n} N_i(\xi, \eta) \cdot x_i \\ y = \sum_{i=1}^{n} N_i(\xi, \eta) \cdot y_i \end{cases} \tag{5.36}$$

Therefore, the computation of the derivatives becomes:

$$\frac{\partial x}{\partial \xi} = \sum_{i=1}^{n} \frac{\partial N_i(\xi, \eta)}{\partial \xi} \cdot x_i$$

$$\frac{\partial x}{\partial \eta} = \sum_{i=1}^{n} \frac{\partial N_i(\xi, \eta)}{\partial \eta} \cdot x_i$$

$$\frac{\partial y}{\partial \xi} = \sum_{i=1}^{n} \frac{\partial N_i(\xi, \eta)}{\partial \xi} \cdot y_i \qquad (5.37)$$

$$\frac{\partial y}{\partial \eta} = \sum_{i=1}^{n} \frac{\partial N_i(\xi, \eta)}{\partial \eta} \cdot y_i$$

This approach enables the construction of a fully general algorithm that can calculate any physical quantity in terms of natural functions and coordinates. These are independent of the specific discretization and finite element definition. Moreover, through the isoparametric formulation, the Jacobian is derived using the same interpolation and shape function derivatives, allowing any quantity to be transformed into the global physical reference system.

5.3 Equivalent Single Layer models

Thanks to the hierarchical expansion of the displacement field along the thickness, by choosing different plunomical basis F_τ and F_s it is possible to incorporate in the proposed FE procedures ESL. The ESL theories are developed by assuming that the displacement field is at least C^1-continuous through the thickness of the laminate. A key feature of ESL models is the adoption of Taylor-like expansions for displacement fields through the thickness of the laminate:

$$\mathbf{u}(x, y, z) = \mathbf{u}_1(x, y) + z\mathbf{u}_2(x, y) + z^2\mathbf{u}_3(x, y) + ... + z^N\mathbf{u}_N(x, y) \qquad (5.38)$$

where $\mathbf{F}_\tau = 1, z, z^2, z^3, ..., z^N$ are the expansion function used to expand the displacement fiel through the thickness.

This approach simplifies the representation of complex interlayer effects and

allows for straightforward integration into finite element analysis.

However, these models oversimplify the mechanical behavior near layer interfaces, potentially underestimating interlaminar stresses and strain discontinuities. Indeed, the major deficiency of the ESL models in modeling composite laminates is that the transverse strain components are continuous across interfaces between dissimilar materials, but the transverse stress components are discontinuous at the layer interfaces.

The final stiffness matrix represents the laminate with equivalent mechanical properties obtained through a homogenization process of the individual layers' characteristics. The stiffness matrix in ESL models is generally more compact and efficient to compute, making it suitable for large-scale problems where computational resources are a concern.

5.4   Layer-Wise models

Layer-Wise models represent a detailed approach to modeling laminated composite structures by treating each individual layer as a distinct mechanical entity. In this approach, the displacement field within each layer is described independetly, allowing for accurate representation of the physical and mechanical properties of each layer, including variations in stiffness, strength, and thermal expansion coefficients. This model directly accounts for the discontinuities in displacement and stress fields at the interfaces between layers, making it highly suitable for analyzing complex multilayered structures where interlaminar stresses and strains are critical.

The LW models use Lagrange polynomials to interpolate displacement variables. The displacement field for a simple plate layer can be expressed as:

$$\mathbf{u} = F_1(\xi)\mathbf{u}_1(x,y) + F_2(\xi)\mathbf{u}_2(x,y) = \frac{1-\xi}{2}\mathbf{u}_1(x,y) + \frac{1+\xi}{2}\mathbf{u}_2(x,y) \quad (5.39)$$

If a parabolic expansion is considered the equation is the following:

$$\mathbf{u} = F_1(\xi)\mathbf{u}_1(x,y) + F_2(\xi)\mathbf{u}_2(x,y) + F_3(\xi)\mathbf{u}_3(x,y) = \quad (5.40)$$

$$= \frac{\xi^2 - \xi}{2}\mathbf{u}_1(x,y) + \frac{1 - \xi^2}{2}\mathbf{u}_2(x,y) + \frac{\xi^2 + \xi}{2}\mathbf{u}_3(x,y)$$

In LW models, the stiffness matrix is constructed by considering each layer of the laminate separately. Each layer has its own material properties and contributes individually to the overall stiffness of the structure. The resulting stiffness matrix in a LW model is typically large and sparse. as shown in Fig. 5.1, reflecting the detailed representation of each layer and the interactions between them. While this approach provides high accuracy, especially for predicting interlaminar stresses, it also requires significant computational resources.

A graphical representation of both ESLm and LWm is provided in Fig. 5.1
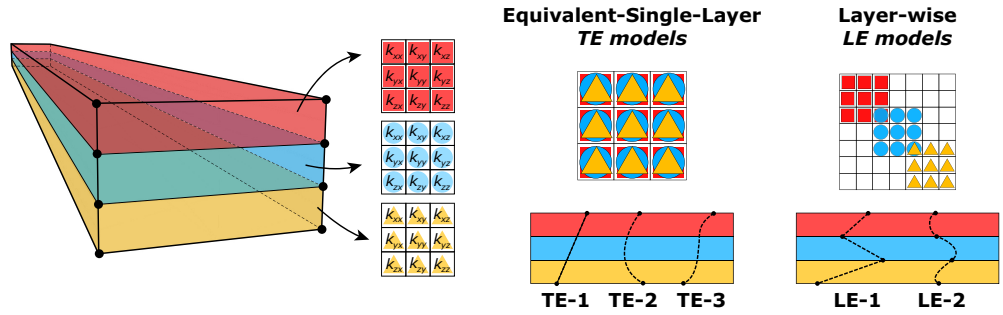
Figure 5.1: ESL and LW models.

5.5 Pure Mechanical Analysis

The analysis of structures deals with very different problems, in terms of boundary conditions and loading configurations. These different kinds of problems can always be solved via variational formulation. The formulation of the problems is strictly related to what kind of work contributions are included, leading to a classification of the structural problems that can be analyzed:

1. **Static analysis**: The load is constant over time, and only the effects of elastic forces and external loads are included. The dimension of the problem is defined by the number of nodes and the degree of freedom of

each node. From the governing equation:

$$\mathbf{Ku} = \mathbf{P} \tag{5.41}$$

The global displacement field is computed, and using the geometrical and constitutive equations, the stress field and the strain field can be computed.

2. **Modal analysis**: This investigates the equilibrium between elastic forces and inertial forces. After substituting the displacement field and strain-displacement relations into the expressions for the potential and kinetic energies, and applying Hamilton's principle, the governing equations of motion for the plate are obtained. These equations describe the free vibration characteristics of the plate.

   After the system equilibrium equations are explicited, it is possible to re-write them in matrix form.

   $$\mathbf{M\ddot{u}}(t) + \mathbf{Ku}(t) = 0 \tag{5.42}$$

   where $\mathbf{M}$ is the mass matrix while $\mathbf{K}$ is the stiffness matrix. Here, a displacement field is assigned, typically a harmonic circular displacement field:

   $$\mathbf{u}(t) = \mathbf{\Phi}e^{i\omega_n t} \rightarrow \mathbf{\ddot{u}}(t) = -\mathbf{\Phi}\omega_n^2 e^{i\omega_n t} \tag{5.43}$$

   Substituting these relations into the governing equation for free vibration analysis it is possible to solve an eigenvalue problem:

   $$\left(\mathbf{K} - \omega^2 \mathbf{M}\right)\mathbf{\Phi} = 0 \tag{5.44}$$

   The solution Eq.5.44 provides a series of eigenvalues $\lambda_i = \omega_n^2$ that represent the natural frequencies of the analyzed structures under the given geometrical boundary conditions. The solution of these equations yields the natural frequencies and mode shapes, which are crucial for understanding the dynamic behavior of the structure.

3. **Frequency Response Problem**: In this case, all inertial forces, elastic forces, and external loads are taken into account. This time, the problem is solved in the frequency domain, considering a harmonic displacement field $\mathbf{u} = \mathbf{u}_0 e^{i\omega t}$ and external load $\mathbf{P} = \mathbf{P}_0 e^{i\omega t}$, which leads to the governing equation in the form:

$$\mathbf{K}\mathbf{u} + \mathbf{M}\ddot{\mathbf{u}} = \mathbf{P} \tag{5.45}$$

$$(\mathbf{K} - \omega^2\mathbf{M})\mathbf{u}_0 = \mathbf{P}_0 \tag{5.46}$$

Finally, for a specific value of ω considered in the investigated frequency range, the final governing equation is equivalent to:

$$\mathbf{u}_0 = (\mathbf{K} - \omega^2\mathbf{M})^{-1}\mathbf{P}_0 \tag{5.47}$$

The dynamic analysis can be seen as a series of static problems, each one associated with a value of ω in a fixed range of frequencies.

Chapter 6

Static Analysis

This chapter aims to analyze a plate structure based on the methodology outlined in [40], implemented in the in-house code by the MUL^2 research group at Politecnico di Torino. The focus is the three-dimensional static and stress analysis of *multilayered* plate structure, *laminated soft core sandwich* plate, and *laminated aluminium honeycomb sandwich with CFRP skins* plate, to assess the capabilities and the accuracy of the present implementation of higher-order model and to detect local through-the-thickness stress distributions.
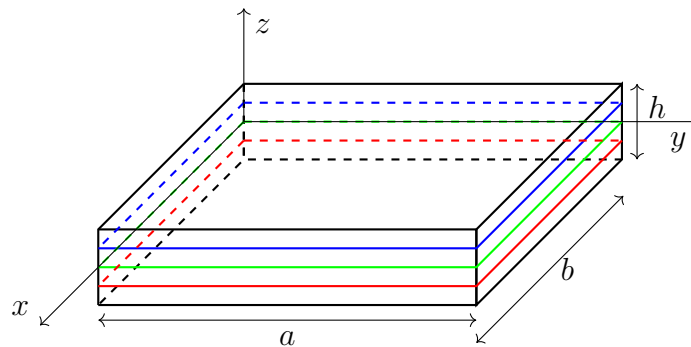

Figure 6.1: Multilayer Plate Model.

6.1 Multi-layer Plate Case

In the context of composite plates, static analysis takes on additional importance due to the complex nature of these structures, which often consist of multiple layers with varying properties. The anisotropic nature of composites laminates, where direction-dependent mechanical properties are considered, makes their analysis more challenging and requires sophisticated modeling techniques. This section analyzes a square plate with length $a = 1\ m$, width $b = a$, and plate slenderness $S = a/h = 4$. The plate shown on Fig. 6.1 consists of $n = 4$ plies of equal thickness $e_i = h/n$ with lamination $[0°, 90°]_s$.

In this case studies clamped (CCCC) boundary conditions are considered. In this way transversal displacements to the mid surface along the edge of the plate are null, but the in-plane coordinates are free.

The mechanical load is a bi-sinusoidal pressure load acting only along the transversal way, applied at the top surface of the plate.

$$
\begin{pmatrix} p_x \\ p_y \\ p_z \end{pmatrix} = \begin{pmatrix} 0 \\ 0 \\ p_z \end{pmatrix} = \begin{pmatrix} 0 \\ 0 \\ p_{z_0} \sin\left(\frac{n\pi x}{a}\right) \sin\left(\frac{m\pi y}{b}\right) \end{pmatrix} \tag{6.1}
$$

In this case study, $n = m = 1$. The maximum amplitude of the pressure will be reach at the center of the plate.

The composite plate is assumed to have transversely isotropic material properties within each ply, with specified values for transversal modulus $E_T = 1$ longitudinal modulus E_L, transverse modulus E_T, shear moduli G_{LT}, G_{TT}, and Poisson's ratios ν_{LT}, ν_{TT}.

$$E_L = 25E_T \quad G_{LT} = 0.5E_T \quad G_{TT} = 0.2E_T \quad \nu_{LT} = \nu_{TT} = 0.25$$

The following table shows the convergence analysis using different expansion model through the thickness. The models implemented are:

- Taylor Complete Linear Model: *TE-1*;

- Taylor Parabolic Model: *TE-2*;

- Taylor Cubic Model: *TE-3*;

- Taylor Quartic Model: *TE-4*;

- Lagrange Cubic Model: *LE-3*.

In this study, these models are selected to capture the increasing complexity of the stress and displacement fields, with higher-order expansions providing more detailed approximations at the cost of increased computational effort and Degrees of Freedom (DOF). The LW models, defined adopting Lagrange's polynomials along the CUF discretization, specifically the cubic Lagrange model (LE-3), is included as an alternative to the Taylor series. The LE-3 model offers a different approach that can provide greater accuracy capturing higher-order kinematics through a LW expansion, which allows to analyse each layer independently.

Mesh	Expansion	DOF	$u_z\left(\frac{a}{2}, \frac{b}{2}, 0\right)$ [m]	$\sigma_{zz}\left(\frac{a}{2}, \frac{b}{2}, 0\right)$ [N/m²]
10 × 10 Q9	TE-1	2646	1.389	0.099
	TE-2	3969	1.385	0.047
	TE-3	5292	1.768	-0.0245
	TE-4	6615	1.769	-0.0421
	LE-3	33075	1.835	-0.0002
15 × 15 Q9	TE-1	5766	1.389	0.1014
	TE-2	8649	1.385	0.0489
	TE-3	11532	1.768	-0.2445
	TE-4	14415	1.769	-0.0420
	LE-3	72075	1.834	-0.0005
20 × 20 Q9	TE-1	10086	1.389	0.1000
	TE-2	15129	1.386	0.0480
	TE-3	20172	1.768	-0.2445
	TE-4	25215	1.769	-0.0422
	LE-3	126075	1.834	-0.0005

Table 6.1: Multi-layer Plate Case. Displacement u_z and Normal Stress σ_{zz} Convergence Study with different Expansion Models.

The analysis shows same type expansion element, LE-3, must be used to ensure stress coerence. The behaviour of stresses is degenerate and higher-order kinematics are required.

Table 6.1 shows the convergence analysis performed by varying the number of elements and the DOF in the finite element mesh. This ensures that the results are accurate and that the chosen models effectively capture the physical behavior of the plate. The analysis coarser to refined discretization model along the plate mid-surface, ranging from 10×10 to 20×20 parabolic element grids, to evaluate the influence of mesh refinement on the accuracy of the results.
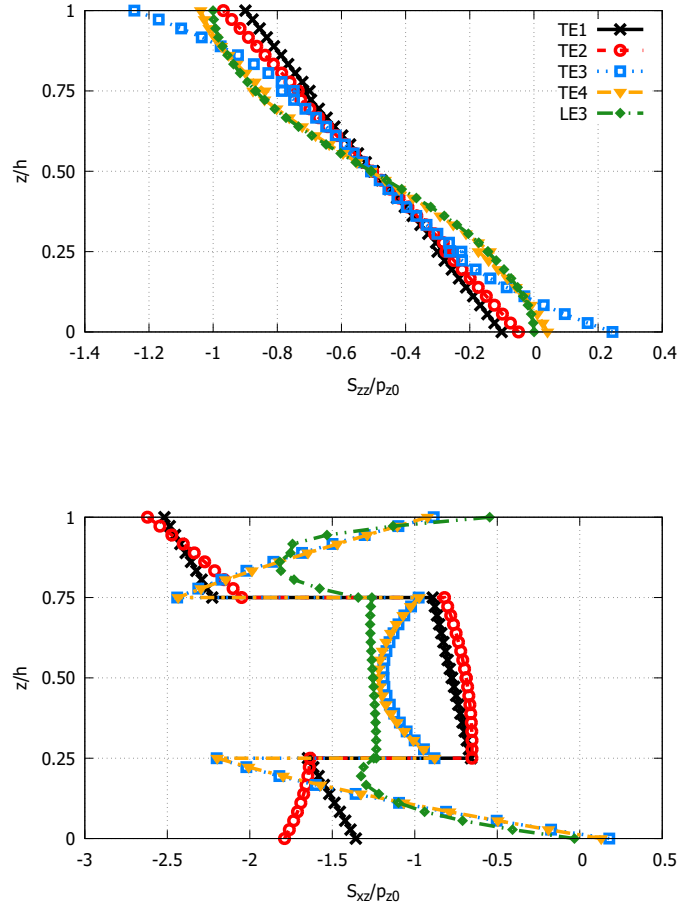

Figure 6.2: Multi-layer Plate Case. Stress distribution along the thickness. Comparison between different Expansion Models.

As the mesh is refined, the displacement values gradually approach a stable value. This demonstrates that the results are not overly dependent on the mesh size but rather on the accuracy of the theory of structure approximation itself.

The behavior of the stress fields, particularly through the thickness of the plate, is examined to assess the accuracy and reliability of each model. The stress distribution exhibits a behavior consistent with the trend illustrated by *Carrera et al.* [40]. Figure 6.2 shows the variation of the normalized stress components (σ_{xz}/p_{z_0}, σ_{zz}/p_{z_0}) across the thickness-to-height ratio z/h. Up to the third-order Taylor expansion (TE), the model is not sufficient to capture the parabolic behavior of transverse shear stresses. For higher-order models, the solution tends to match the Lagrange expansion (LE), which ensures compatibility at the plate ends and continuity of stresses across the interfaces between the layers.

6.2 Laminated Soft Core Sandwich Plate

As second case study, the static analysis of a laminated sandwich plate subjected to different boundary conditions is here presented. The set up of this numerical investigation is based on the studies proposed by *Chalak et al.* [41], where a square and simmetric laminated plate of lateral sides $a = b = 1 \ m$, plate slenderness $S = a/h = 10$, and 20×20 Q9 element mesh, is proposed.
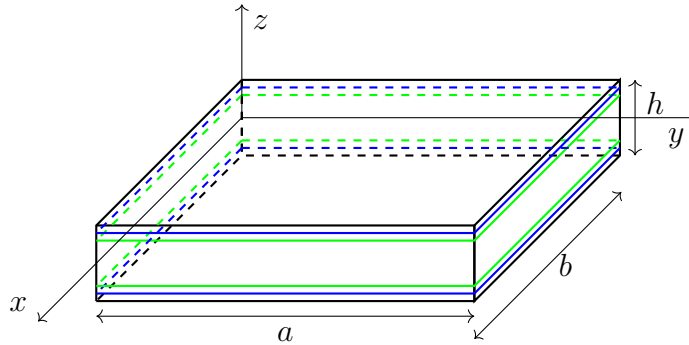

Figure 6.3: Laminated Soft Core Sandwich Plate Model.

In this case, the face sheets ($h_f = 0.1h$) are made of orthotropic materials arranged in a symmetric layup, providing strength and rigidity, while the core ($h_c = 0.8h$) is made of a softer, more compliant material, in a global stacking sequence $[0°/90°/Core/90°/0°]$.

Properties	Face Sheet Material	Core Material
E_1 $[GPa]$	276.0	0.5776
E_2 $[GPa]$	6.9	0.5776
E_3 $[GPa]$	6.9	0.5776
G_{12} $[GPa]$	4.14	0.1079
G_{13} $[GPa]$	3.45	0.22215
G_{23} $[GPa]$	4.14	0.1079
ν_{12}	0.25	0.0025
ν_{13}	0.25	0.0025
ν_{23}	0.33	0.00345
ρ $[kg/m^3]$	681.8	1000

Table 6.2: Laminated Soft Core Sandwich Plate Case. Properties of the Face Sheet and Core Materials. [41]

The core material, characterized by lower stiffness compared to the face sheets, plays a critical role in distributing shear forces and preventing buckling, thereby enhancing the overall structural integrity of the plate.

Tab.2: Laminated Soft Core Sandwich Plate Case. Properties of the Face Sheet and Core Materials.

In the first numerical case, a convergence analysis is carried out considering as boundary condition the clamped (CCCC) and clamped-free-free-free (CFFF) boundary conditions. As the previous case, to investigate the mechanical response of the plate and the three-dimensional stress state induced by this stacking sequence configuration, the plate is subjected to a bi-sinusoidal pressure load applied at the top surface.
Only one type of expansion model (LE-3) was investigated, since its capability of capture the behavior of complex plates.

The following analysis, illustrated in Fig. 6.4 and Fig. 6.5, presents the normal and shear stress distributions of the sandwich plate under different boundary conditions and at various points. Notably, the normal stress component σ_{xx} stands out for its significantly higher values compared to σ_{zz}. In the core of the laminate, σ_{zz} exhibit an almost linear distribution, unlike the behavior observed in the multilayer laminated plate. This difference arises from the soft core, which plays a pivotal role in redistributing the applied load.

Figure 6.4: Laminated Soft Core Sandwich Plate Case. Stress distribution along the thickness in (a/4,a/4) with CCCC boundary conditions.

6.3 Laminated Aluminium Honeycomb Sandwich Plate with CFRP skins

The static analysis of a sandwich plate featuring a honeycomb core of aluminum 5052 and outer skins of CFRP is crucial for understanding its load-bearing capabilities and overall structural integrity. This section analyzes a square and simmetric sanswich plate, with length $a = 1\ m$, width $b = a$ and plate slenderness $S = a/h = 10$.

The global stacking sequence ($[0°/90°/Core/90°/0°]$) and thickness distribution of skins and core are identical as the previous plate, with $h_f = 0.1h$ and $h_c = 0.8h$. The honeycomb unit cell follow the same metrics of [42], as shown in Figure 6.6, where a regular honeycomb structure is chosen. Thus, $c = l$ and $\theta = 30°$ [39].

(a)

(b)

(c)

(d)

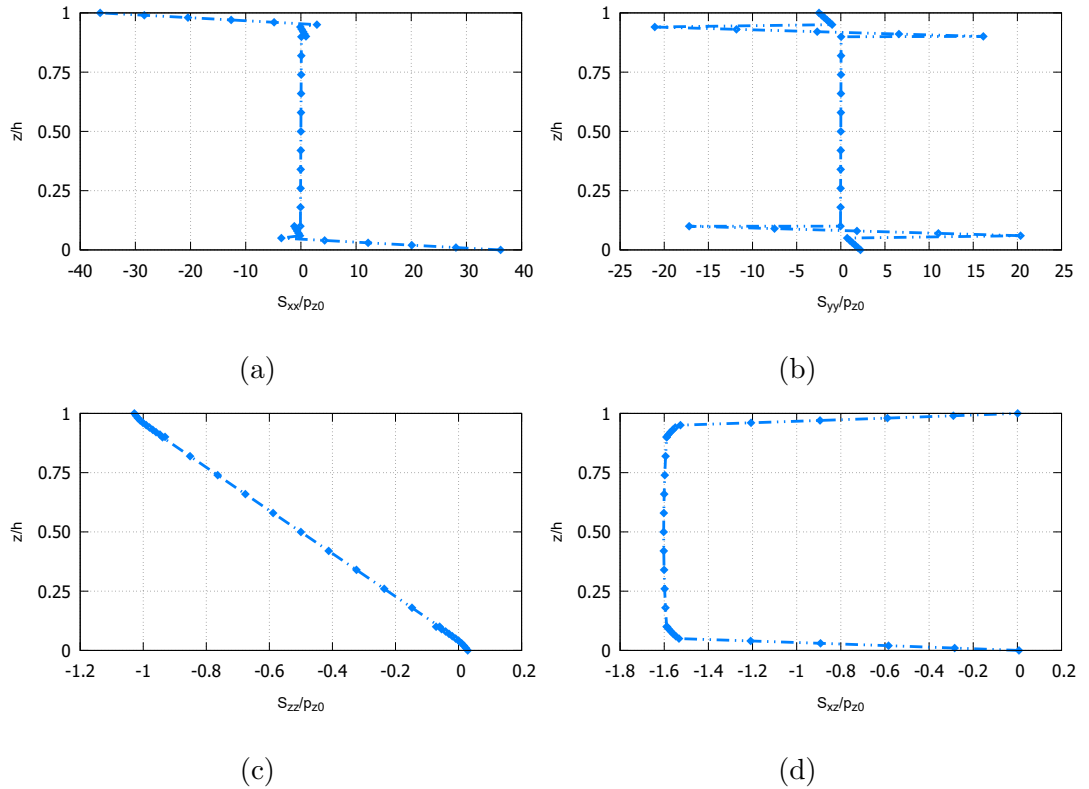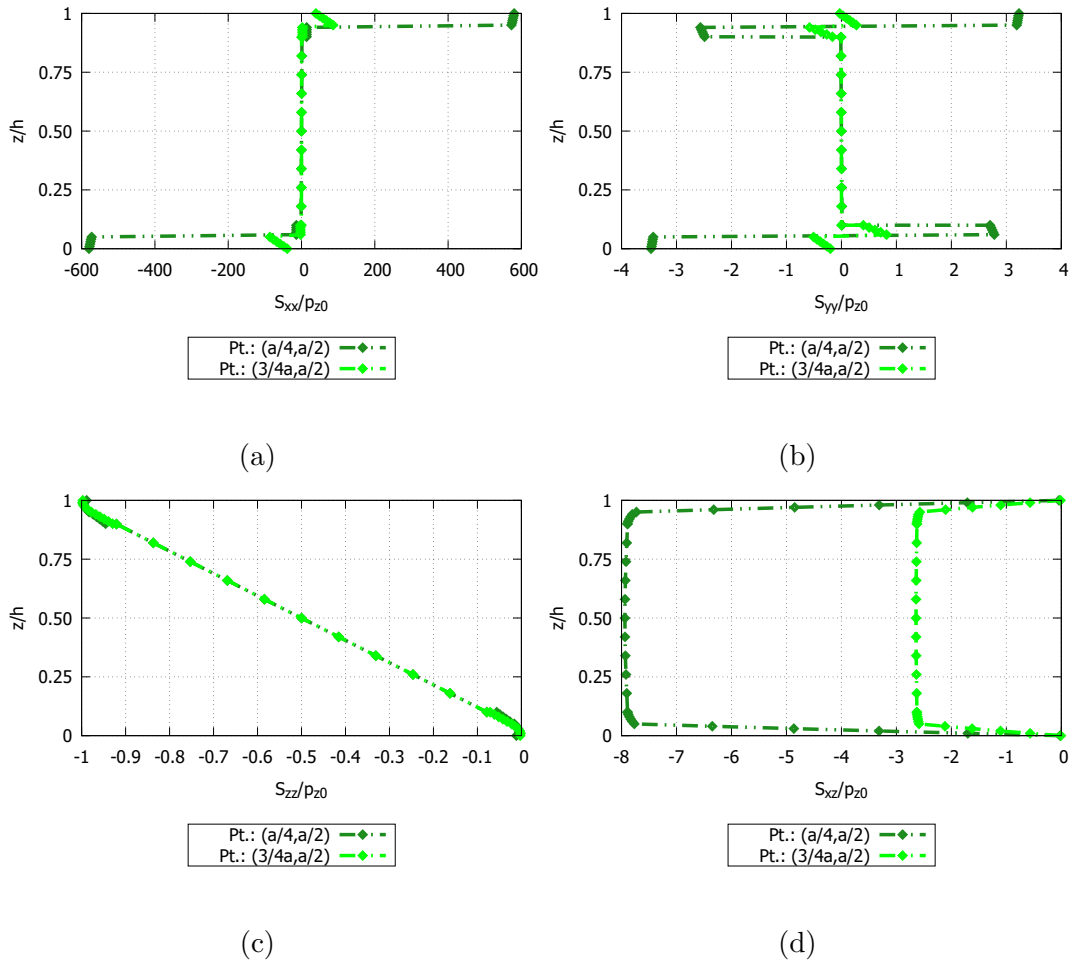Figure 6.5: Laminated Soft Core Sandwich Plate. Stress distribution along the thickness with CFFF boundary conditions.
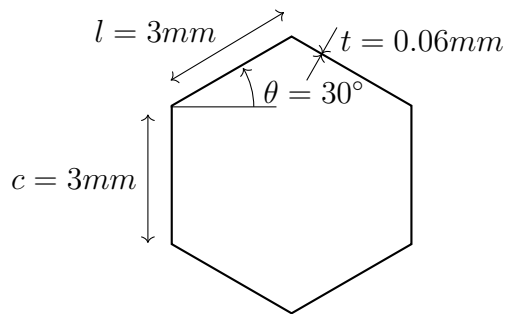

Figure 6.6: Geometric parameters of the unit cell.

The properties of CFRP and Al-5052 honeycomb core are listed in Table 6.3. The in-plane and out-of-plane equivalent elastic properties of the honeycomb

core are obtained using equations outlined in Section 4.4.

A static analysis was performed comparing the model with 10 LE-3 and 10 TE-4, with a 20×20 parabolic element mesh. The stress distributions in Figure 6.7 reveal critical characteristics of the laminated aluminum honeycomb sandwich structure with CFRP skins. The pronounced discontinuities in the normal stresses (σ_{xx} and σ_{yy}) at the skin-core interfaces indicate regions of high stress concentration, which are potential initiation points for debonding or delamination. This behavior is typical of anisotropic materials like CFRP due to their directional stiffness and strong orthotropic properties.

Property	CFRP [43]	Al-5052 Honeycomb
E_1	108 $[GPa]$	1.29 $[MPa]$
E_2	8 $[GPa]$	1.29 $[MPa]$
E_3	8 $[GPa]$	2155.4 $[MPa]$
G_{12}	4 $[GPa]$	0.81 $[MPa]$
G_{13}	4 $[GPa]$	300.22 $[MPa]$
G_{23}	3 $[GPa]$	450.33 $[MPa]$
ν_{12}	0.32	0.98
ν_{13}	0.32	1.98E-04
ν_{23}	0.3	1.98E-04
ρ $[kg/m^3]$	1560	83.14

Table 6.3: Properties of the unidirectional laminate face sheet (CFRP) and Al-5052 Honeycomb core.

Tab.1: Properties of the unidirectional laminate face sheet (CFRP) and Al-5052 Honeycomb core.

The stress profiles (σ_{zz} and σ_{xz}) display smooth gradients across the core for LE-3, while the TE-4 model fails to ensure continuity of stresses across the interfaces between the layers. However, the high stresses at layer interface reaffirm the importance of ensuring robust adhesion to mitigate interfacial failure.
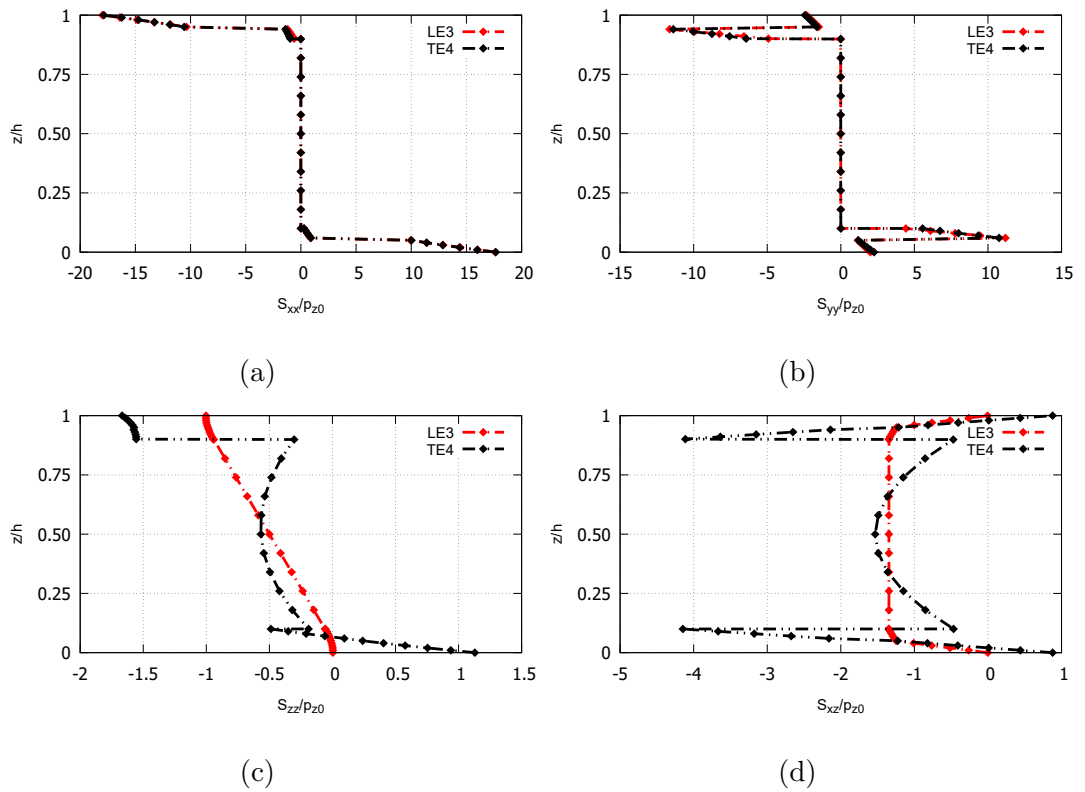
Figure 6.7: Laminated Aluminium Honeycomb Sandwich with CFRP skins Case. Stress distribution along the thickness in (a/4,a/4) with CCCC condition and LE-3 and TE-4 Expansions.

Chapter 7

Modal Analysis

This chapter focuses on the modal analysis of structural components, leveraging FE models to study their dynamic behavior. The primary aim is to evaluate the natural frequencies and mode shapes of multi-layer and sandwich plates. In the context of laminated soft core sandwich plates, special attention is given to the convergence properties of the FE models, ensuring their reliability and accuracy.

Through a systematic investigation, the chapter explores the impact of varying material properties, geometrical configurations, and modeling approaches (e.g., ESL and LW) on the dynamic behavior of these structures, forming the groundwork for subsequent vibro-acoustic analyses.

7.1 Laminated Soft Core Sandwich Plate Case

Free vibration analysis of laminated soft core sandwich plates structures builds the framework for predicting their response to dynamic load by computing their natural frequencies and corresponding mode shapes. This analysis is particularly important in space applications, where the avoidance of *resonance* is crucial to maintaining structural integrity and functionality over extended mission durations.

7.1.1 Convergence Analysis

The modal analysis of the laminated sandwich plate presented in Sec. 6.2 is proposed. This benchmark problem has been extensively analyzed by *Chalak et al.* [41], and the numerical solutions obtained by the proposed high order 2D plate model are compared with the literature results proposed by the authors. The capabilities of the present implementation of higher-order 2D plate models in the computation of natural frequencies and mode shapes are here assessed, measuring the efficiency and accuracy by the total DOF required by the numerical simulation and relative percentage difference.

Mesh	Mode	TE1	TE2	TE3	TE4
	1	$27.9731^{(148\%)}$	$27.8893^{(148\%)}$	$13.5228^{(20.1\%)}$	$13.5037^{(19.9\%)}$
	2	$45.0860^{(169\%)}$	$44.8214^{(168\%)}$	$19.3072^{(15.3\%)}$	$19.2815^{(15.1\%)}$
10×10	3	$46.3378^{(143\%)}$	$46.0803^{(142\%)}$	$23.6043^{(24\%)}$	$23.5668^{(23.8\%)}$
Q9	4	$58.5622^{(157\%)}$	$58.0584^{(155\%)}$	$26.8506^{(17.8\%)}$	$26.8159^{(17.6\%)}$
	5	$67.3971^{(185\%)}$	$66.7216^{(182\%)}$	$27.4363^{(16.1\%)}$	$27.3953^{(15.9\%)}$
	6	$69.7566^{(147\%)}$	$69.1068^{(145\%)}$	$33.2600^{(18\%)}$	$33.2127^{(17.8\%)}$
DOF		2646	3969	5292	6615
	1	$27.9713^{(148\%)}$	$27.8866^{(148\%)}$	$13.3819^{(18.8\%)}$	$13.3610^{(18.7\%)}$
	2	$45.0763^{(169\%)}$	$44.8111^{(168\%)}$	$19.0370^{(13.7\%)}$	$19.0080^{(13.5\%)}$
20×20	3	$46.3283^{(143\%)}$	$46.0703^{(142\%)}$	$23.3173^{(22.5\%)}$	$23.2777^{(22.3\%)}$
Q9	4	$58.5482^{(157\%)}$	$58.0441^{(155\%)}$	$26.3580^{(15.6\%)}$	$26.3191^{(15.4\%)}$
	5	$67.3475^{(185\%)}$	$66.6724^{(182\%)}$	$27.0686^{(14.5\%)}$	$27.0245^{(14.3\%)}$
	6	$69.7073^{(147\%)}$	$69.0579^{(145\%)}$	$32.7146^{(16\%)}$	$32.6634^{(15.9\%)}$
DOF		10086	15129	20172	25215
	1	$27.9713^{(148\%)}$	$27.8866^{(148\%)}$	$13.3819^{(18.8\%)}$	$13.3610^{(18.7\%)}$
	2	$45.0763^{(169\%)}$	$44.8111^{(168\%)}$	$19.0370^{(13.7\%)}$	$19.0080^{(13.5\%)}$
30×30	3	$46.3283^{(143\%)}$	$46.0703^{(142\%)}$	$23.3173^{(22.5\%)}$	$23.2777^{(22.3\%)}$
Q9	4	$58.5482^{(157\%)}$	$58.0441^{(155\%)}$	$26.3580^{(15.6\%)}$	$26.3191^{(15.4\%)}$
	5	$67.3475^{(185\%)}$	$66.6724^{(182\%)}$	$27.0686^{(14.5\%)}$	$27.0245^{(14.3\%)}$
	6	$69.7073^{(147\%)}$	$69.0579^{(145\%)}$	$32.7146^{(16\%)}$	$32.6634^{(15.9\%)}$
DOF		22326	33489	44652	55815

Table 7.1: Laminated Soft Core Sandwich Plate Case. Modes convergence study with different mesh refinement using Taylor Expansion models.

Tables 7.1 and 7.2 show the non-dimensional natural frequencies ($\bar{\omega} = 100\omega a\sqrt{\rho_c/E_2}$) obtained for different mid-surface FE discretization and

different theory of structure approximation adopted in the mathematical model, investigating the first six frequencies. The table categorizes the results based on the type of expansion models.

Mesh	Mode	LE1	LE2	LE3
	1	$11.8407^{(5.151\%)}$	$11.8376^{(5.123\%)}$	$11.8371^{(5.119\%)}$
	2	$16.5299^{(1.282\%)}$	$16.5255^{(1.308\%)}$	$16.5241^{(1.317\%)}$
10×10	3	$20.9904^{(10.252\%)}$	$20.9839^{(10.218\%)}$	$20.9829^{(10.213\%)}$
Q9	4	$22.8024^{(0.003\%)}$	$22.7952^{(0.029\%)}$	$22.7911^{(0.047\%)}$
	5	$24.0429^{(1.698\%)}$	$24.0353^{(1.666\%)}$	$24.0336^{(1.659\%)}$
	6	$28.8049^{(2.170\%)}$	$28.7948^{(2.135\%)}$	$28.7910^{(2.121\%)}$
DOF		14553	27783	41013
	1	$11.6971^{(3.875\%)}$	$11.6936^{(3.844\%)}$	$11.6922^{(3.832\%)}$
	2	$16.2845^{(2.748\%)}$	$16.2795^{(2.778\%)}$	$16.2767^{(2.794\%)}$
20×20	3	$20.6825^{(8.635\%)}$	$20.6750^{(8.596\%)}$	$20.6721^{(8.581\%)}$
Q9	4	$22.3519^{(1.973\%)}$	$22.3441^{(2.007\%)}$	$22.3386^{(2.031\%)}$
	5	$23.6751^{(0.143\%)}$	$23.6664^{(0.106\%)}$	$23.6626^{(0.090\%)}$
	6	$29.2278^{(3.670\%)}$	$28.2686^{(0.268\%)}$	$28.2627^{(0.247\%)}$
DOF		55473	105903	156333
	1	$11.6971^{(3.875\%)}$	$11.6936^{(3.844\%)}$	$11.6922^{(3.832\%)}$
	2	$16.2845^{(2.748\%)}$	$16.2795^{(2.778\%)}$	$16.2767^{(2.794\%)}$
30×30	3	$20.6825^{(8.635\%)}$	$20.6750^{(8.596\%)}$	$20.6721^{(8.581\%)}$
Q9	4	$22.3519^{(1.973\%)}$	$22.3441^{(2.007\%)}$	$22.3386^{(2.031\%)}$
	5	$23.6750^{(0.142\%)}$	$23.6664^{(0.106\%)}$	$23.6626^{(0.090\%)}$
	6	$29.2278^{(3.670\%)}$	$28.2686^{(0.268\%)}$	$28.2627^{(0.247\%)}$
DOF		122793	234423	346053

Table 7.2: Laminated Soft Core Sandwich Plate Case. Modes convergence study with different mesh refinement using Lagrange Expansion models.

The frequencies were computed using three progressively refined meshes. The coarse mesh provides initial estimates of the frequencies. However, the relatively large elements lead to less accurate results due to the lower resolution in capturing the plate's deformation. The medium-density mesh significantly improves the resolution, leading to more accurate frequency predictions. The finer mesh shows that the frequency values have converged, as there is minimal difference between the results of the 20×20 and 30×30 parabolic element grids. This convergence suggests that the solution is becoming independent of the mesh size, affirming that the results are reliable.
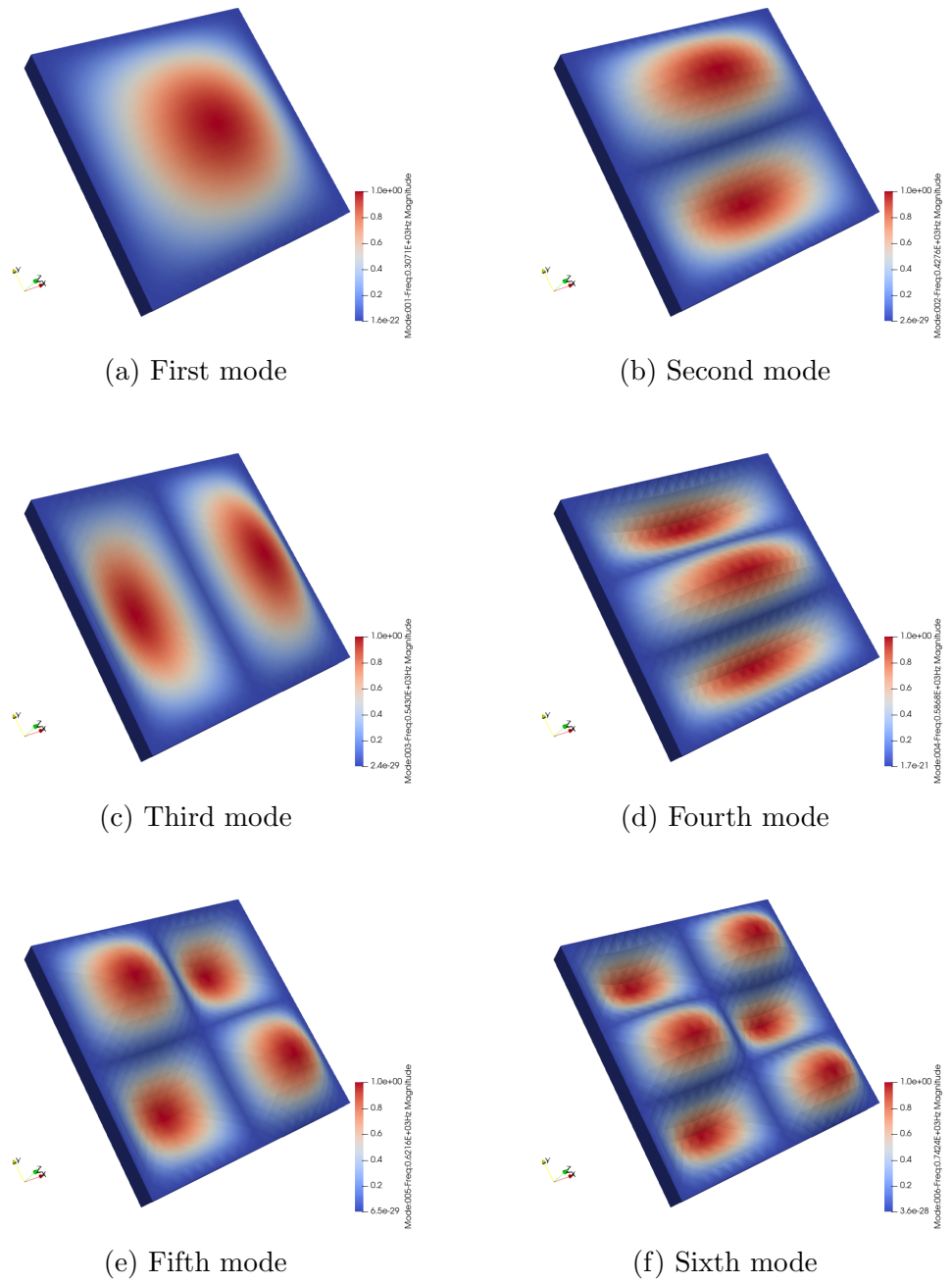
(a) First mode

(b) Second mode

(c) Third mode

(d) Fourth mode

(e) Fifth mode

(f) Sixth mode

Figure 7.1: Laminated Soft Core Sandwich Plate Case. First six modes for CCCC boundary condition with LE-3 expansion model and 20×20 mesh size.

The frequencies obtained using *Taylor Expansion model* (TE-1, TE-2, TE-3, TE-4) show consistent convergence as the mesh is refined. For instance, the first frequency for TE-2 starts at 27.8893 for the 10×10 mesh, slightly adjusts to 27.8866 for the 20×20 mesh, and remains stable at this value for the 30×30 mesh. As the order increases, the frequencies converge more closely to the benchmark values, starting from 27.9713 for TE-1 and reaching 13.3610 for TE-4 in the 30×30 mesh. However, the Taylor series expansion models, in particular the lower orders, while useful for initial approximations, tend to provide less accurate results, as seen from the relative error percentage. This stems from the structure configuration itself, considering that laminated plates require high order models that can ensure C^0 continuity condition.

LW models (LE-1, LE-2, LE-3) offer more refined and accurate results, and show a faster convergence with mesh refinement. This reflects the higher accuracy and robustness of LW models in capturing the vibrational behavior of the plate.

7.1.2   Influence of Boundary Conditions

The dynamic behavior of laminated sandwich plates is dependent on the boundary conditions imposed. This section explores how different boundary conditions influence the non-dimensional natural frequencies of a laminated soft core sandwich plate. Table 7.3 lists the frequencies for the first six vibration modes under four different boundary conditions:

- CCCC (Clamped-Clamped-Clamped-Clamped);

- SSSS (Simply Supported-Simply Supported-Simply Supported-Simply Supported);

- CFCF (Clamped-Free-Clamped-Free):

$$
\begin{cases}
x = 0 & u_x, u_y, u_z = 0 \\
x = 1 & u_x, u_y, u_z = 0
\end{cases}
\tag{7.1}
$$

- CFFF (Clamped-Free-Free-Free)

	CCCC		SSSS		CFCF		CFFF	
Mode	Present	Ref.[41]	Present	Ref.[41]	Present	Ref.[41]	Present	Ref.[41]
1	11.6922	11.2730	10.2720	9.8364	6.4097	7.0434	3.7449	2.9732
2	16.2767	16.7652	14.2907	15.5115	7.3424	7.7323	4.4488	3.6067
3	20.6721	19.0637	17.6533	18.0886	12.9646	14.2286	10.7136	9.4038
4	22.3386	22.8320	20.4558	21.7089	14.3542	15.2589	12.4583	10.7278
5	23.6626	23.6763	20.5765	22.2181	18.5439	17.1217	12.4024	15.8498
6	28.2627	28.2354	25.2668	26.9350	20.0221	21.3709	13.4984	17.2328

Table 7.3: Laminated Soft Core Sandwich Plate Case. Comparison between CUF-Model non-dimensional frequencies and reference frequencies under various boundary conditions.

The results were compared with reference solutions available in the literature, taken from [41]. The CCCC configuration provides the highest stiffness, resulting in the highest frequencies across all modes. The first mode frequency, for example, is 11.6922, which is the highest among the configurations studied. The SSSS condition allows for rotational movement at the edges but prevents translational displacement. This results in lower stiffness and, consequently, lower frequencies than the CCCC condition. The first mode frequency under SSSS is 10.2720, reflecting the increased flexibility of the plate.

Mode	CCCC	SSSS	CFCF	CFFF
1	307.12803	252.79834	256.34113	98.37134
2	427.55514	374.41916	269.19913	116.85975
3	543.01051	376.96805	401.35449	281.42359
4	586.78788	450.97908	514.98411	327.25315
5	621.56642	478.37733	531.18734	325.78525
6	742.40025	523.85234	537.46781	354.57516

Table 7.4: Laminated Soft Core Sandwich Plate Case. Frequencies in Hz under various boundary conditions.

The CFCF boundary condition, with alternating clamped and free edges, provides an intermediate level of stiffness. The first mode frequency is 9.7587, indicating that the mixed boundary conditions lead to a moderate level of structural stiffness. In the CFFF condition, only one edge is clamped, with the remaining edges free. This results in the lowest stiffness among the boundary conditions studied, leading to relatively low frequencies, with the first mode

frequency at 3.7449.

The discrepancies between the present and reference results highlight the sensitivity of frequency predictions to the modeling techniques and assumptions used. The differences could arise from several factors, as numerical methods and boundary condition implementation.
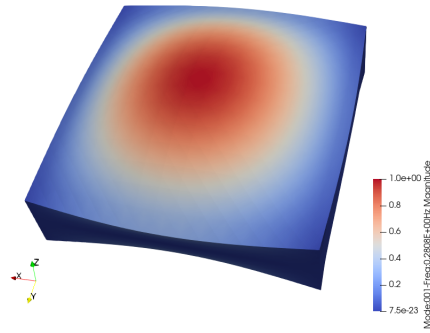
7.2 Multi-layer Plate Case and Laminated Aluminium Honeycomb Sandwich Plate with CFRP skins Case

The modal analysis of the multi-layer plate and laminated aluminium honeycomb sandwich plate presented in Sec. 6.1 and Sec. 6.3, respectively, is suggested. Building on the promising results obtained from the previous analysis of the laminated soft-core sandwich plate, the first six modes are obtained using the LE-3 expansion (8 LE-3 for the multi-layer plate and 10 LE-3 for the laminated honeycomb sandwich plate) with a 20×20 Q9 element grid.

Mode	Multilayer Plate	Laminated Honeycomb Sandwich Plate
1	0.281	670.711
2	0.354	1300.187
3	0.354	1301.100
4	0.504	1846.969
5	0.528	2185.329
6	0.676	2204.284

Table 7.5: Multi-layer Plate Case and Laminated Honeycomb Sandwich Plate. Frequencies in Hz under CCCC boundary condition.

The results show that the sandwich plate with a honeycomb core exhibits significantly higher modal frequencies compared to the multi-layer plate. This highlights the superior dynamic stiffness of the sandwich configuration and confirms the suitability of sandwich plates for applications requiring high dynamic performance, particularly where vibration reduction and structural stability are key priorities.
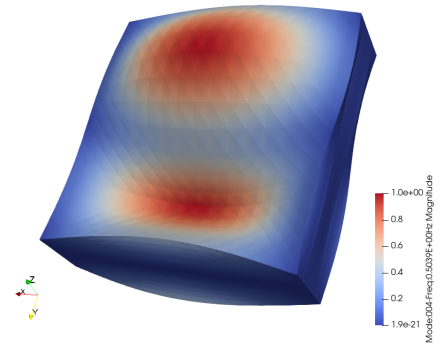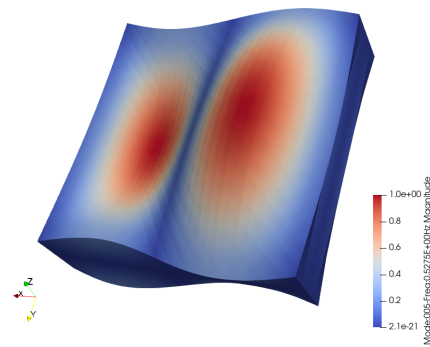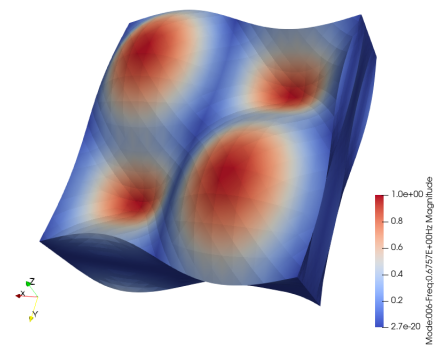
(a) First mode
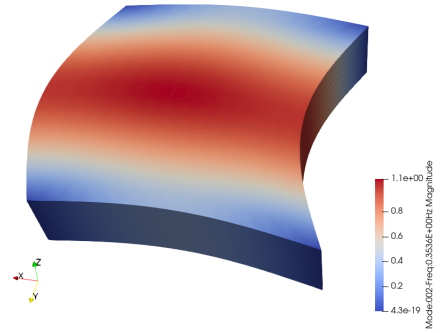
(b) Second mode
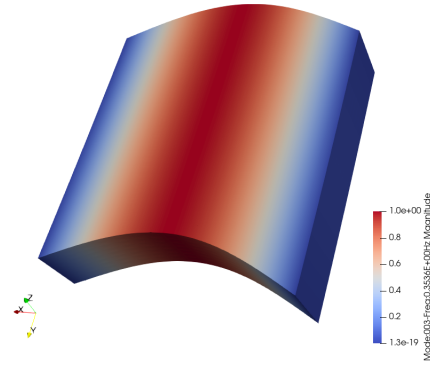
(c) Third mode

(d) Fourth mode

(e) Fifth mode

(f) Sixth mode

Figure 7.2: Multi-layer Plate Case. First six modes for CCCC boundary condition with LE-3 expansion model and 20×20 mesh size.
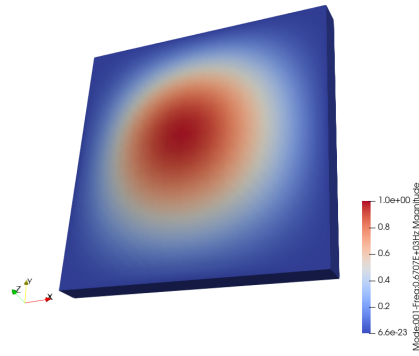
71

(a) First mode

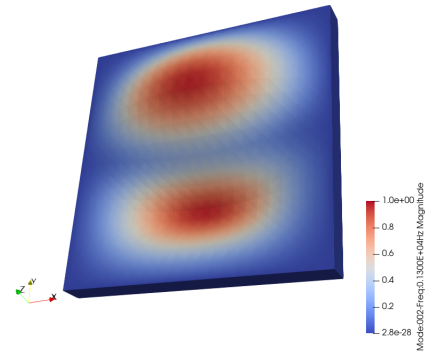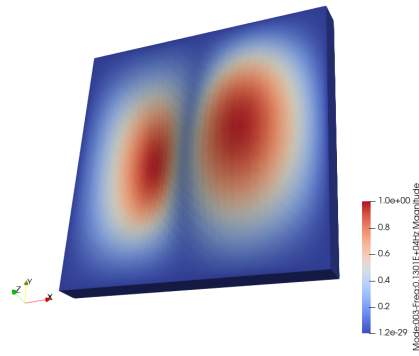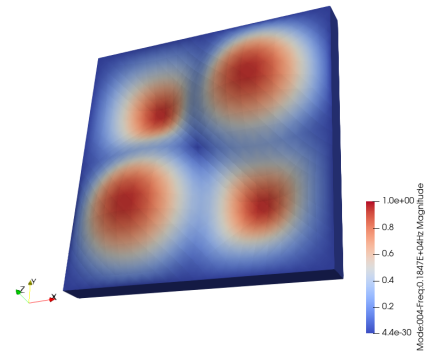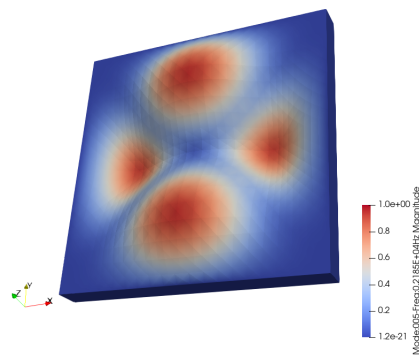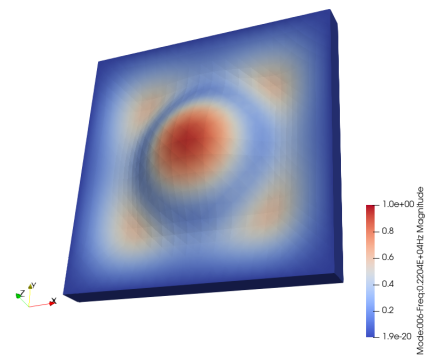(b) Second mode

(c) Third mode

(d) Fourth mode

(e) Fifth mode

(f) Sixth mode

Figure 7.3: Laminated Aluminium Honeycomb Sandwich Plate with CFRP skins Case. First six modes for CCCC boundary condition with LE-3 expansion model and 20×20 mesh size.

Chapter 8

Frequency Response Problem

The frequency response analysis of plates subjected to uniform pressure loads is a critical step in understanding their dynamic behavior. Building upon the modal analysis discussed in the previous chapter, where natural frequencies and mode shapes were evaluated, this study explores the response of a square plate under varying boundary conditions and pressure loads. Utilizing FE models, dynamic simulations are conducted for pressure loads ranging from 8 Pa to 32 Pa. Special emphasis is placed on the interplay between boundary constraints and loading conditions, offering deeper insights into the structural performance under dynamic excitation.

8.1   Convergence Analysis

This section focuses on the frequency response analysis of the laminated soft core sandwich plate extensively studied in Chapter 6 and in Chapter 7. The study examines three boundary conditions: CCCC, CFCF, CFFF. These boundary conditions allow for a systematic evaluation of how different levels of constraint influence the plate's dynamic behavior.
The accuracy of Finite Element Analysis (FEA) in predicting the natural frequencies of a structure depends heavily on the refinement of the mesh used to discretize the domain. In this study, three progressively refined meshes were employed to analyze the frequency response of the square plate under varying boundary conditions: 10×10 and 20×20 Q9 element grids.

Mesh	Expansion	DOF	(x, y)	BC	p_{ref} (Pa)	MAX Displacement u_z (mm)	Frequency (Hz)
10 Q9	10 LE-3	41013	0.5, 0.5	CCCC	8	-0.00349	312
					16	-0.00699	312
					32	-0.0139	312
				CFCF	8	-0.00167	261
					16	0.00399	258
					32	0.00798	258
						-0.00319	405
				CFFF	8	639000	0
						-0.0974	3
						0.00898	103
					16	5120000	0
						-0.779	3
						0.0718	306
					32	2560000	0
						-0.389	3
						0.0359	306
20 Q9	10 LE-3	156333	0.5, 0.5	CCCC	32	0.0131	306
				CFCF	32	-0.0205	99
						0.0199	327
				CFFF	32	6520000	0
						-0.389	3
						-0.0368	306

Table 8.1: Laminated Soft Core Plate Case. Maximum Displacement for Different Boundary Conditions and Pressure Loads with 10×10 and 20×20 Mesh refinement.

The results show that, while the 10×10 mesh can provide rough estimates, lacking the resolution needed for reliable frequency predictions, the 20×20 mesh achieves a good balance between computational efficiency and accuracy. Notably, some peaks in the displacement response coincide with, or are close to, the natural frequencies obtained from the modal analysis. It can be observed that the peak at 306 Hz in Fig. 8.1, for the most refined mesh, closely matches the frequency of the first mode, as reported in Table 7.4. For the other boundary conditions, however, this correspondence is less evident.

The high displacement values observed for the CFFF boundary condition are a result of the boundary condition itself, which significantly affects the stiffness and dynamic response of the structure. This can lead to phenomena such as resonance or localized deformation effects.
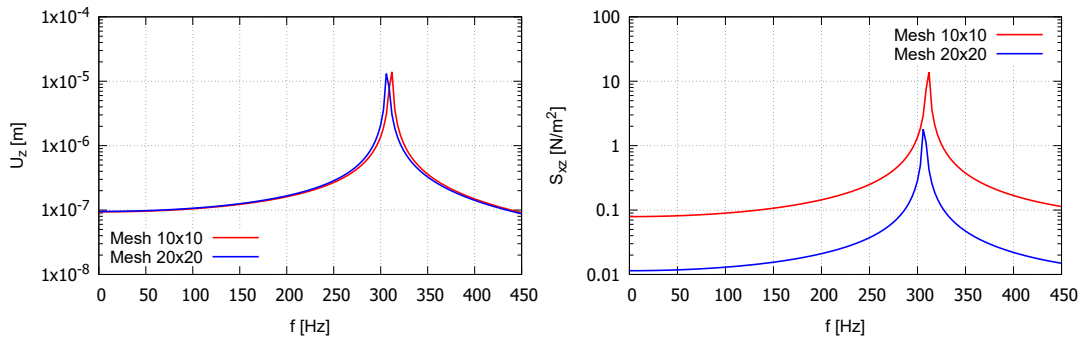
Figure 8.1: Laminated Soft Core Sandwich Plate Case. Displacement and Stress for Different Mesh Refinements with CCCC Boundary Condition.
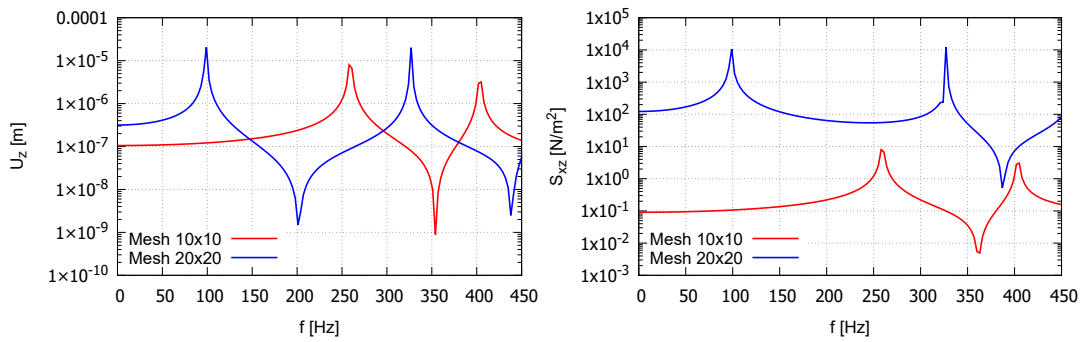

Figure 8.2: Laminated Soft Core Sandwich Plate Case. Displacement and Stress for Different Mesh Refinements with CFCF Boundary Condition.
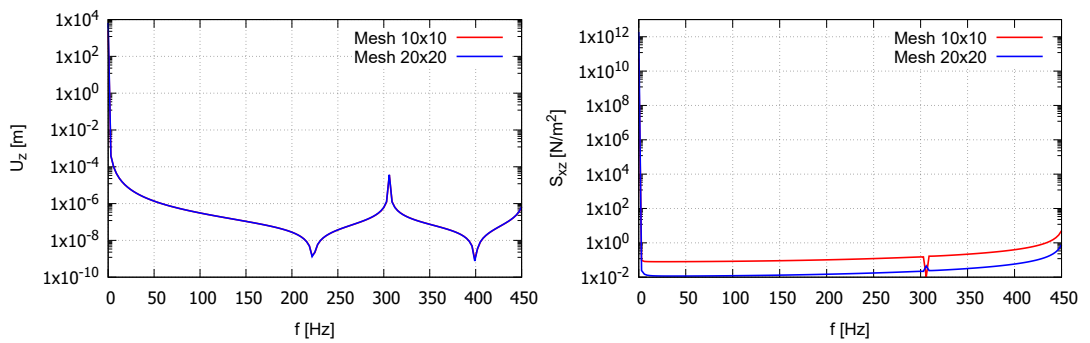

Figure 8.3: Laminated Soft Core Sandwich Plate Case. Displacement and Stress for Different Mesh Refinements with CFFF Boundary Condition.

Chapter 9

Power Spectral Density Analysis

The prediction of sandwich structures response to acoustic excitation, particularly the SPL under random or periodic loads, is critical in many noise and vibration control scenarios. This chapter provides a detailed analysis of the SPL behavior of sandwich panels under various loading conditions, focusing on the modeling of pressure loads and power spectral densities (PSDs).

9.1 Theoretical Background

9.1.1 Consistent vs. Lumped-Load Approximation

In the case of linear systems, the random response of a structure can be efficiently predicted using a frequency domain approach. This method utilizes the PSD of the excitation force, as well as the system's FRF, to compute the cross-PSD of the structural response.

Accurately converting continuous random loads into discrete nodal forces for finite element analysis is crucial. Two common approaches are usually employed for discretizing random loads [44]: *lumped-load* and *consistent-load* approximations.

In the *lumped-load method*, random loads are applied to nodal points by multiplying the area surrounding the node with the distributed force. This approach assumes that the forces in the vicinity of the node are fully correlated and may require a finer mesh to achieve acceptable accuracy, increasing the computational cost.

The *consistent-load approach* consider the shape functions used in finite element analysis to interpolate the distributed load across the element. This ensures that the random load is distributed more accurately between nodes, taking into account the spatial correlations of the random field and rotational DOFs. This method requires fewer elements for the same level of accuracy compared to the lumped-load method.

9.1.2   Formulation of Consistent Random Loads

The formulation of consistent load differ for *deterministic* and *random* loads. For a deterministic load, the consistent load vector for a pressure load applied over an element is expressed as:

$$\mathbf{F}(t) = \sum_{i=1}^{NE} \mathbf{T}_i \int_{A_i} \mathbf{N}^T \mathbf{p}_i(t) \, dA_i \qquad (9.1)$$

Where:

- $\mathbf{N}$ represents the shape function matrix,

- $\mathbf{p}(t)$ is the pressure load applied at any point on the element,

- A_i denotes the area of the element.

- $\mathbf{T}$ is the Boolean matrix which maps the local degrees of freedom to the global degrees of freedom.

- NE is the total number of elements.

For random loads, the key challenge is accounting for the spatial correlation between different points on the surface of the structure. The cross-PSD matrix of the consistent load vector can be derived similarly, using the random nature of the excitation. The correlation between two instants of random excitation is given by:

$$R_{FF}(\tau) = E \sum_{i=1}^{NE} \sum_{j=1}^{NE} \mathbf{T}_i \int_{A_i} \int_{A_j} \mathbf{N}_i^T \mathbf{Q}_i \mathbf{P}_i(t) \mathbf{P}_i(t+\tau) \mathbf{Q}_j^T \mathbf{N}_j \, dA_i \, dA_j \mathbf{T}_j^T \quad (9.2)$$

By taking the Fourier transform of the correlation function, the cross-PSD matrix of the nodal loads can be expressed as:

$$S_{FF}(\omega) = \sum_{i=1}^{NE} \sum_{j=1}^{NE} \mathbf{T}_i \int_{A_i} \int_{A_j} \mathbf{N}_i^T \mathbf{Q}_i \mathbf{S}_{P_i P_j}(\omega) \mathbf{Q}_j^T \mathbf{N}_j \, dA_i \, dA_j \mathbf{T}_j^T \qquad (9.3)$$

Where:

- $\mathbf{S}_{P_i P_j}$ is the cross-PSD of the pressure load of elemts i and j,

- $S_{FF}(\omega)$ is the cross-PSD matrix of the nodal forces.

9.1.3 Application in Finite Element Models

The consistent-load approach has been implemented in FE software to improve the accuracy of random vibration analyses. The method involves calculating the excitation cross-PSD matrix, which is used to derive the PSD of the structural displacements and stresses. The PSDs of the three- dimensional displacement components, S_{u_i}, and stress components, S_{σ_j}, at different frequencies ω, are related to the PSD of the load, S_{FF}, as expressed by the following equations [45]:

$$S_{u_i}(\omega) = \bar{\mathbf{H}}_{u_i}(\omega) S_{FF}(\omega) \bar{\mathbf{H}}_{u_i}^T(\omega), \quad i = 1, 2, 3 \qquad (9.4)$$

$$S_{\sigma_j}(\omega) = \bar{\mathbf{H}}_{\sigma_j}(\omega) S_{FF}(\omega) \bar{\mathbf{H}}_{\sigma_j}^T(\omega), \quad j = 1, \ldots, 6 \qquad (9.5)$$

Here, $\bar{\mathbf{H}}(\omega)$ represents the complex conjugate of admittance matrix, and $\bar{\mathbf{H}}^T(\omega)$ denotes its transpose. These matrices are computed through FE methods, which yields the admittance matrix as part of the generalized force vector $\mathbf{F}$, and for any non-zero generalized coordinate k, the matrix $\mathbf{H}_{q_k}(\omega)$ is defined as:

$$\mathbf{H}_{q_k}(\omega) = [q_{k1}, q_{k2}, \ldots, q_{kL}], \quad k = 1, \ldots, nnz, \quad L = 1, \ldots, f_s \qquad (9.6)$$

Here, f_s refers to the number of frequency steps considered. The column vector q_k captures the DOF of the FE model, derived from the following expression:

$$q_k(\omega) = \left[-\omega^2 \mathbf{M} + i\omega \mathbf{C} + \mathbf{K} \right]^{-1} F_k^*, \quad i = \sqrt{-1} \qquad (9.7)$$

The vector F_k^* contains a single non-null element, equal to 1, representing the non-zero term of the generalized force vector $\mathbf{F}$. $\mathbf{M}$, $\mathbf{C}$, and $\mathbf{K}$ correspond to the mass, damping, and stiffness matrices of the FE model, respectively. To reduce the computational cost, an uncoupled modal reduction strategy is commonly used, allowing the arbitrary selection of eigenvectors ($\mathbf{x_j}$) that are derived from the undamped, homogeneous equation of motion:

$$\left[-\omega_j^2 \mathbf{M} + \mathbf{K} \right] \mathbf{x}_j e^{i\omega t} = 0, \quad j = 1, \dots, nm \tag{9.8}$$

By selecting eigenvectors and organizing them into a $DoF \times nm$ matrix $\mathbf{X}$, Eq. 9.7 can be rewritten as:

$$\mathbf{X}^T q_k(\omega) = \left[-\omega^2(\mathbf{X}^T\mathbf{M}\mathbf{X}) + i\omega(\mathbf{X}^T\mathbf{C}\mathbf{X}) + (\mathbf{X}^T\mathbf{K}\mathbf{X}) \right]^{-1} \mathbf{X}^T F_k^* \tag{9.9}$$

9.2 Random Load Excitation

In this study, three distinct cases of laminated plate structures were analyzed under random load excitation to investigate their dynamic response characteristics. The plates were subjected to a white noise and the random load was modeled through 25 concentrated forces evenly distributed across the top surface, following the same method as the model proposed by *Filippi et al.* [45]. For each case, the dynamic response was analyzed by plotting key metrics such as the displacement U_z and the shear stress σ_{xz} PSDs as functions of frequency. The model adopted in this study is the LE-3 for each layer, which was chosen for its ability to effectively capture the mechanical behavior of laminated plates under dynamic loading conditions, as seen in the previous sections. Specifically, the analysis employed 10 LE-3 for the sandwich plates and 8 LE-3 for the multilayer plate. This choice ensures a sufficient level of refinement to accurately model the complex stress and deformation distributions inherent to these structures.

9.2.1 Multi-Layer Plate Case

The PSDs of the displacement and shear stress show that the peak response occurs at very low frequencies, which could pose a potential issue. This be-

havior, associated with a lower natural frequency as discussed in Sec. 7.2, lead to unwanted dynamic amplification under low-frequency excitations.
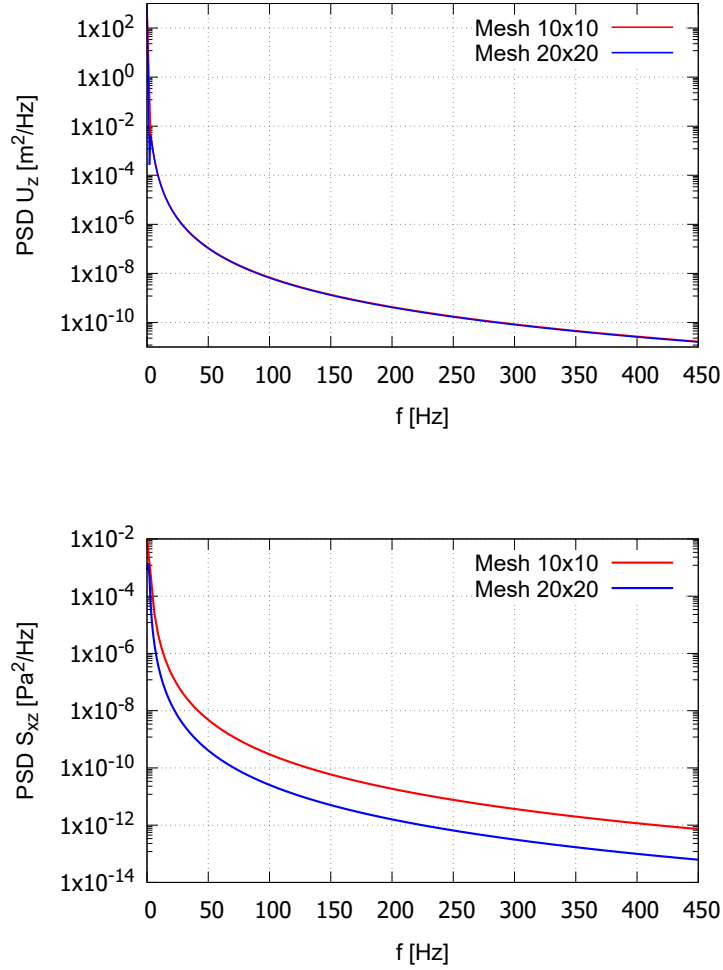

Figure 9.1: Multi-Layer Plate Case. Displacement and Stress PSDs for Different Mesh Refinements with CCCC Boundary Condition.

9.2.2 Laminated Soft Core Plate Case

The plots shows a steep increase near the resonance frequency, followed by a sharp drop beyond it. This indicates that the soft core allows significant shear deformation, reflecting a localized concentration of stress in the material, and displacement.
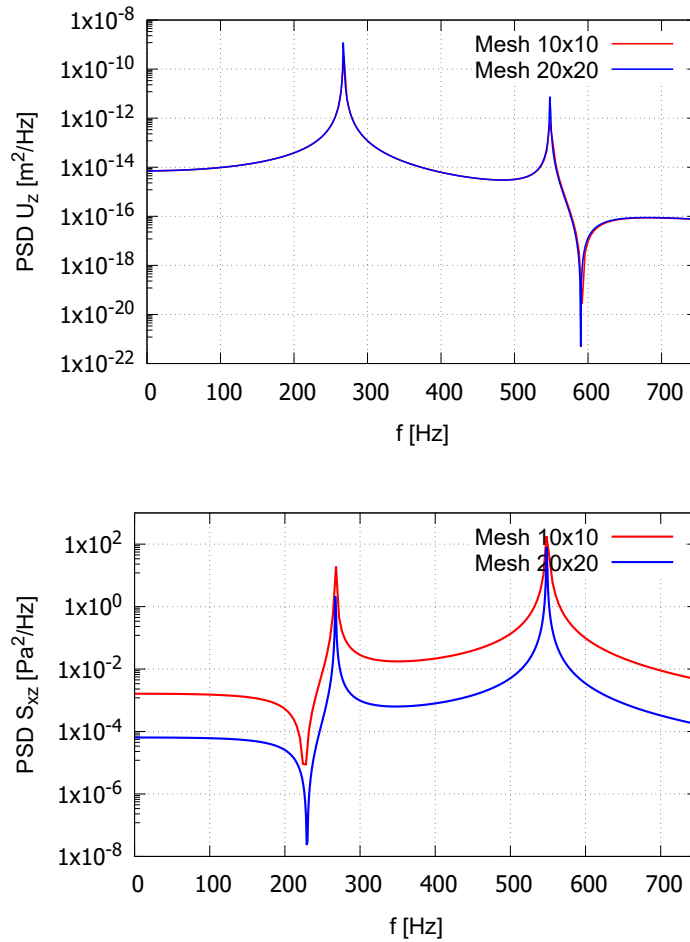
Figure 9.2: Laminated Soft Core Sandwich Plate Case. Displacement and Stress PSDs for Different Mesh Refinements with CCCC Boundary Condition.

9.2.3 Laminated Aluminium Honeycomb Sandwich Plate Case

The presence of multiple resonance peaks at higher frequencies reflects the complex dynamic modes of the honeycomb structure, where stiffness dominates the response. The plot for shear stress exhibits several distinct peaks corresponding to the resonance frequencies. These peaks indicate that while the honeycomb design efficiently localizes stresses, the structure also experiences high shear stress concentrations at specific frequencies, particularly in modes where out-of-plane deformation is significant.
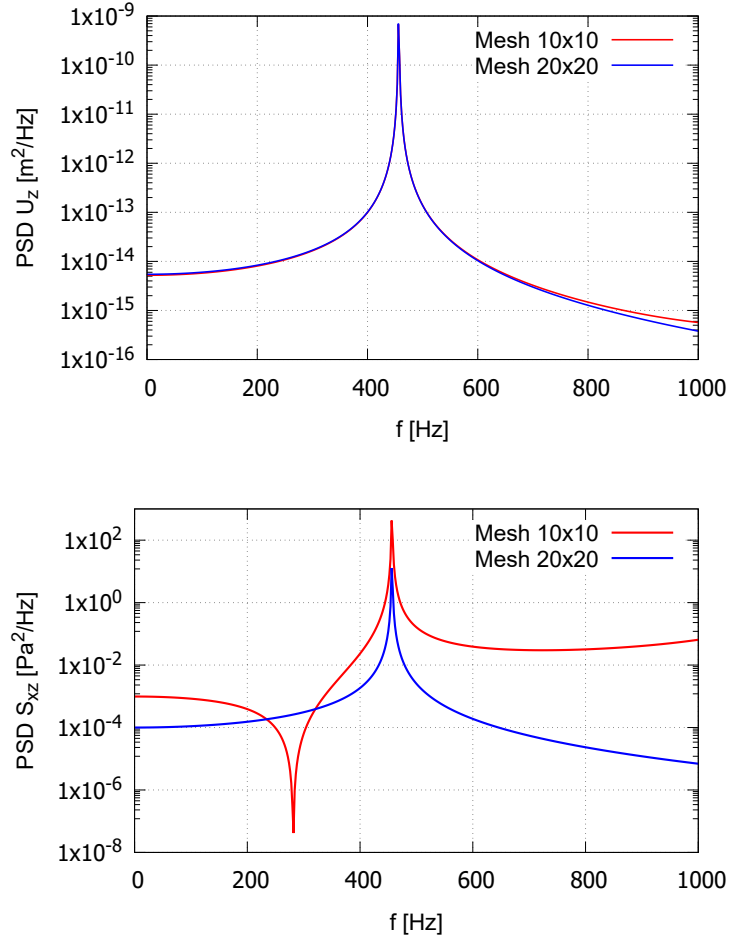
81

Figure 9.3: Laminated Aluminium Honeycomb Sandwich Plate Case. Displacement and Stress PSDs for Different Mesh Refinements with CCCC Boundary Condition.

9.3 SPL Analysis

The proposed computational model enables the analysis of the structural response to an acoustic load simulated through a PSD model, derived from the sound pressure level of Vega-C envelope spectrum noise [46], and dynamic frequency-domain analysis, considering CCCC boundary conditions and varying material properties. The results illustrate how the structural response is influenced by the chosen theory and kinematics.

To ensure convergence and optimize the computational cost of the simulations,
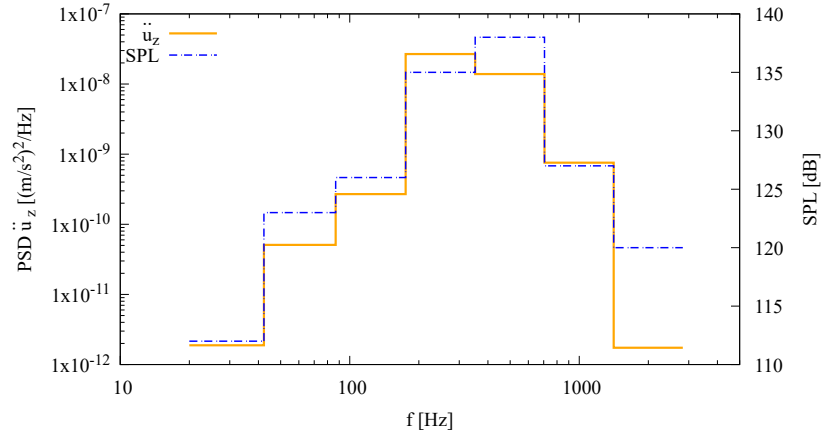
Figure 9.4: Laminated Sandwich Soft Core Plate Case. Acceleration PSD under Vega-C enviroment.
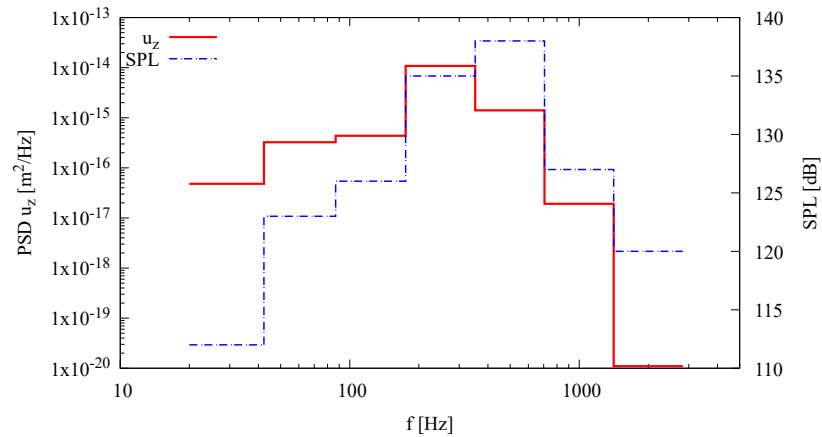

Figure 9.5: Laminated Sandwich Soft Core Plate Case. Displacement PSD under Vega-C enviroment.

the structure was modeled using previously validated approaches. Specifically, a 20×20 parabolic element mesh was employed in the plane, and parabolic LE-type models were applied along the thickness. This choice ensures compatibility criteria for transverse normal and shear stresses at the interfaces. This aspect becomes particularly critical in the dynamic analysis of honeycomb and laminated structures, especially sandwich-type configurations, where the structural behavior is significantly affected by shear effects.

For both structures, analyses reveal a strong dependency on the material prop-

erties. In particular, the results, obtained applying Vega-C pressure spectrum, show an acoustic response characterized by different modes excitation for each plate. Consequently, in this context, the material dependency of the acoustic response becomes a critical design parameter. By adjusting material properties or honeycomb characteristics, it is possible to tailor material behavior to either amplify or suppress specific structural behaviors deemed undesirable.
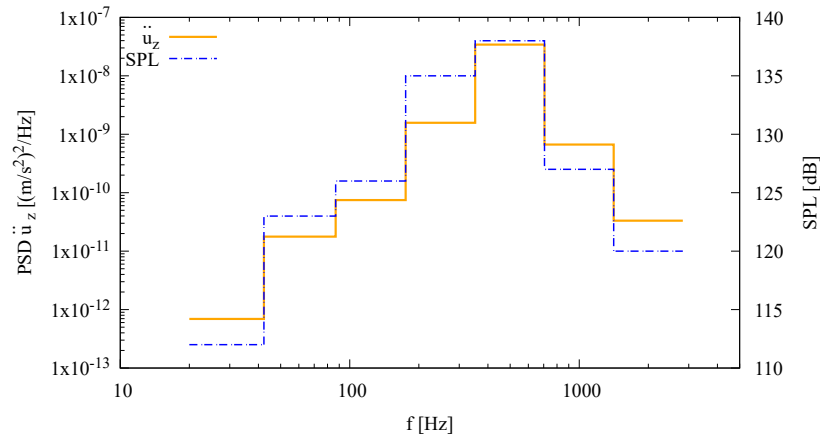

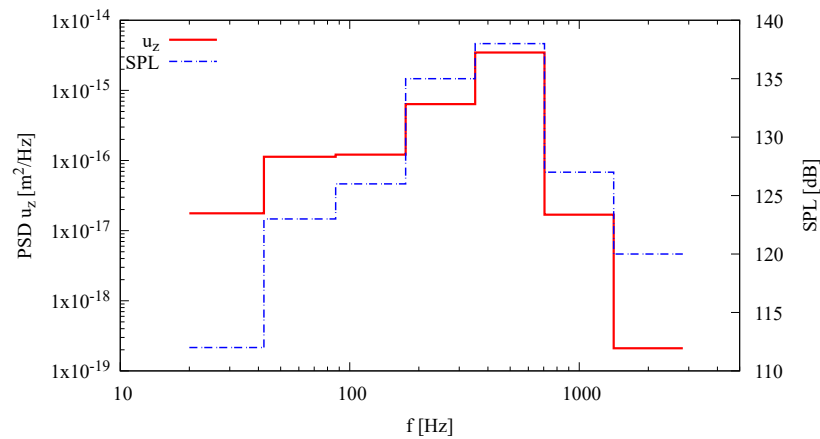Figure 9.6: Laminated Aluminium Sandwich with CFRP skins Case. Acceleration PSD under Vega-C enviroment.

Figure 9.7: Laminated Aluminium Sandwich with CFRP skins Case. Displacement PSD under Vega-C enviroment.

The area under the Power Spectral Density (PSD) curve is a key parameter that represents the energy content for both acceleration and displace-

ment. This parameter offers valuable insights into the energy distribution across the frequency domain, providing essential information for analyzing vibrations and the dynamic response of the structure. For the sandwich soft core, the displacement energy is $4.086 \times 10^{-12} \mathrm{m}^2$, while the acceleration energy is $3.859 \times 10^{-5} \mathrm{m}^2/\mathrm{s}^4$. In the case of the sandwich honeycomb core, the displacement energy increases to $7.403 \times 10^{-12} \mathrm{m}^2$, and the acceleration energy is $3.046 \times 10^{-5} \mathrm{m}^2/\mathrm{s}^4$.

Based on the analyses conducted, it can be concluded that material dependency, particularly the influence of lamination sequences or material types, is a fundamental aspect of designing these structures. Comparing the structural responses of honeycomb and sandwich configurations under identical boundary conditions reveals similar response mechanics.

Chapter 10

Conclusion and Future Developements

This thesis has conducted a thorough vibroacoustic analysis of multilayer and laminated sandwich panels tailored for space applications, addressing both their structural and acoustic performance. Using a higher-order 2D plate finite element model implemented in the MUL^2 code developed at Politecnico di Torino, the study effectively captured the complex mechanical behavior of these advanced structures. The goal of this research was to evaluate the dynamic and acoustic characteristics of multi-layer and laminated sandwich plates, with a focus on their application in environments where both structural integrity and noise control are critical, such as aerospace settings.

The study began with static and modal analyses, which provided foundational insights into the mechanical performance of the panels, and assessed the computational model. The static analyses of three different configurations of laminated plates, a *multi-layer plate* with a symmetric $[0, 90]_s$ lamination, a *laminated soft-core sandwich plate*, and a *laminated aluminum honeycomb sandwich plate with CFRP skins*, were evaluated. Overall, the static analyses demonstrated the effectiveness of LW expansion models, particularly LE-3, in capturing the complex mechanical responses of laminated sandwich plates. The study also underscored the critical role of material selection, structural configuration, and adhesion quality in determining the performance of sandwich structures, particularly in demanding aerospace environments.

The modal analysis provided a detailed understanding of how laminated plates respond to different dynamic loads, offering insights that are vital for optimizing the design of structures subjected to high-frequency vibrations. The results obtained using the higher-order 2D plate model were compared with existing literature, such as the work by *Chalak et al.* [41], and demonstrated good agreement with the reference data. The use LW models showed faster convergence compared to the ESL models, which, while useful in the initial stages of the calculation, were less efficient for higher-order solutions. The results indicated that the sandwich plate with a honeycomb core and the sandwich plate with a soft core exhibited significantly higher modal frequencies than the multi-layer plate, confirming the superior dynamic stiffness of the sandwich configuration. This is particularly important for applications requiring high dynamic performance, such as vibration reduction and structural stability during launch or operational use in space.

The dynamic analysis further enriched the understanding of the panels' behavior under dynamic loading. One of the most interesting observations was the correlation between the displacement peaks and the natural frequencies identified in the modal analysis for certain boundary conditions. Additionally, the dynamic analysis highlighted the importance of boundary conditions in the design process, as resonance phenomena or localized deformation effects can occur in different configurations.

The findings highlight the critical importance of accurate modeling of random loads and their distribution within the context of sandwich and laminated structures. Comparative analyses of different configurations, in terms of dynamic response and SPL, demonstrate how the selection of materials and boundary conditions significantly influences structural behavior.

Despite its comprehensive approach, this study has certain limitations. The analyses do not account for non-linear phenomena that could arise under extreme conditions, such as large deformations or material plasticity. Moreover, the study did not consider the effects of variable environmental factors such

as temperature fluctuations or vacuum conditions typical in space. These factors can significantly alter the mechanical and acoustic-response behavior of structures, and their incorporation into future models would lead to more robust predictions. Furthermore, the acoustic analysis was based on idealized scenarios, which may differ from the actual operational conditions experienced in space, such as coupled acoustic-structural interactions during launch and in orbit. Experimental validation, coupled with these extended analyses, could further refine the accuracy of the numerical models and improve the design process.

In conclusion, this thesis has provided significant contributions to the understanding of the vibro-acoustic performance of laminated sandwich panels for space applications. The study has successfully demonstrated that these configurations offer superior mechanical properties, including enhanced stiffness and vibration damping, and that LW models effectively capture their complex behavior.

Bibliography

[1] "MIL-STD-1540C: Test Requirements for Launch, Upper-Stage and Space Vehicles," United States Air Force Military Standard, Tech. Rep., 1994.

[2] V. D'Alessandro, G. Petrone, F. Franco, and S. De Rosa, "A review of the vibroacoustics of sandwich panels: Models and experiments," *Journal of Sandwich Structures and Materials*, vol. 15, pp. 541–582, Sep. 2013. DOI: 10.1177/1099636213490588.

[3] J. S. Archer, "Nasa space vehicle design criteria/structures/ - structural vibration prediction," NASA, Tech. Rep. NASA-SP-8050, 1970, NASA Report.

[4] NASA, "Acoustic Noise Requirement," NASA Preferred Reliability Practices, United States, Tech. Rep. PD-ED-1259, May 1996, Available at: https://llis.nasa.gov/lesson/787.

[5] J. Panda, *Aeroacoustics of space vehicles*, Presentation at Applied Modeling & Simulation (AMS) Seminar Series, NASA Ames Research Center, Moffett Field, CA, Apr. 2014.

[6] Component Analysis Branch, Systems Dynamics Laboratory, Science and Engineering, "Design and Verification Guidelines for Vibroacoustic and Transient Environments," NASA Technical Memorandum, George C. Marshall Space Flight Center, Tech. Rep. NASA-TM-86538, 1986.

[7] K. Eldred, "Acoustic loads generated by the propulsion system," NASA, Tech. Rep. NASA-SP-8072, 1971, NASA Report.

[8] C. Lubert, K. Gee, and S. Tsutsumi, "Supersonic jet noise from launch vehicles: 50 years since nasa sp-8072," *The Journal of the Acoustical Society of America*, vol. 151, no. 2, pp. 752–791, 2022.

[9] H. Himelblau, D. L. Kern, J. E. Manning, A. G. Piersol, and S. Rubi, "Nasa handbook 7005: Dynamics environmental criteria," NASA, Washington, DC, Tech. Rep. NASA-HDBK7005, 2001.

[10] B. J. Greska, A. Krothapalli, J. M. Seiner, B. Jansen, and L. Ukeiley, "The effects of microjet injection on an f404 jet engine," in *Proceedings of the AIAA Conference*, 2005.

[11] C. M. Fuller, H. Himelblau, and T. D. Scharton, "Assessment of space vehicle aeroacoustic-vibration prediction, design, and testing," NASA, Tech. Rep. NASA-CR-1596, 1970, NASA Contract Report.

[12] T. Sarafin, P. Doukas, L. Demchak, and M. Browning, *Part 1: Introduction to vibration testing*, 2014.

[13] R. H. Lyon, *Statistical energy analysis of dynamical systems*. MIT press Cambridge, MA, 1975.

[14] T. Sarafin, P. Doukas, L. Demchak, and M. Browning, *Part 5: Random vibration testing*, 2016.

[15] S. Community. "Direct field acoustic noise testing (dfan)." Accessed: July 2024. [Online]. Available: `https://community.sw.siemens.com/s/article/direct-field-acoustic-noise-testing-dfan`.

[16] "NASA-STD-7001B: Payload Vibroacoustic Test Criteria," NASA, Tech. Rep. NASA-STD-7001A, 2017, NASA Technical Standard.

[17] "Payload Test Requirements," NASA, Tech. Rep. NASA-STD-7002, 2017, NASA Technical Standard.

[18] U. Farooq, M. Ahmad, S. Rakha, N. Ali, A. Khurram, and T. Subhani, "Interfacial mechanical performance of composite honeycomb sandwich panels for aerospace applications," *Arabian Journal for Science and Engineering*, vol. 42, Sep. 2016. DOI: `10.1007/s13369-016-2307-z`.

[19] J. Kee Paik, A. K. Thayamballi, and G. Sung Kim, "The strength characteristics of aluminum honeycomb sandwich panels," *Thin-Walled Structures*, vol. 35, no. 3, pp. 205–231, 1999, ISSN: 0263-8231. DOI: `https://doi.org/10.1016/S0263-8231(99)00026-9`. [Online]. Available: `https://www.sciencedirect.com/science/article/pii/S0263823199000269`.

[20] G. Sun, D. Chen, H. Xintao, G. Zheng, and Q. Li, "Experimental and numerical studies on indentation and perforation characteristics of honeycomb sandwich panels," *Composite Structures*, vol. 184, Jan. 2018. DOI: `10.1016/j.compstruct.2017.09.025`.

[21] H. Composites, *Hexweb tm, datasheet "honeycomb attributes and properties"*, 2008.

[22] E. A. Piana, C. Petrogalli, D. Paderno, and U. Carlsson, "Application of the wave propagation approach to sandwich structures: Vibro-acoustic properties of aluminum honeycomb materials," *Applied Sciences*, vol. 8, no. 1, 2018, ISSN: 2076-3417. DOI: `10.3390/app8010045`. [Online]. Available: `https://www.mdpi.com/2076-3417/8/1/45`.

[23] *Studying the Mechanisms of High Rates of Tool Wear in the Machining of Aramid Honeycomb Composites*, vol. Volume 2: Additive Manufacturing; Materials, International Manufacturing Science and Engineering Conference, Jun. 2017, V002T03A002. DOI: 10.1115/MSEC2017-2694. eprint: https://asmedigitalcollection.asme.org/MSEC/proceedings-pdf/MSEC2017/50732/V002T03A002/2519385/v002t03a002-msec2017-2694.pdf. [Online]. Available: https://doi.org/10.1115/MSEC2017-2694.

[24] F. Loffredo, E. Vardaci, D. Bianco, A. Di Nitto, and M. Quarto, "Radioprotection for astronauts' missions: Numerical results on the nomex shielding effectiveness," *Life*, vol. 13, no. 3, 2023, ISSN: 2075-1729. DOI: 10.3390/life13030790. [Online]. Available: https://www.mdpi.com/2075-1729/13/3/790.

[25] H. Composites, *Hexweb tm, product data sheet "hexweb® hrh-10"*, 2014. [Online]. Available: https://www.hexcel.com/Resources/DataSheets/Honeycomb.

[26] X. Huang, X. Hu, J. Guo, D. Zhang, S. Yao, L. Zhan, B. Ma, M. Huang, and L. Zhang, "Aramid honeycomb cores under constant pressure: Unveiling the out-of-plane compression deformation," *Polymers*, vol. 16, no. 14, 2024, ISSN: 2073-4360. DOI: 10.3390/polym16141974. [Online]. Available: https://www.mdpi.com/2073-4360/16/14/1974.

[27] J. Lindsey, "Space antennas from advanced composite materials," in *1985 Antennas and Propagation Society International Symposium*, vol. 23, 1985, pp. 613–616. DOI: 10.1109/APS.1985.1149457.

[28] H. Composites, *Hexweb tm, product data sheet "hexweb® hrh-49®"*, 2014. [Online]. Available: https://www.hexcel.com/Resources/DataSheets/Honeycomb.

[29] H. F. Seibert, "Applications for pmi foams in aerospace sandwich structures," *Reinforced plastics*, vol. 50, no. 1, pp. 44–48, 2006.

[30] A. Shi, G. Zhang, and C. Zhao, "Study of rigid cross-linked pvc foams with heat resistance," *Molecules*, vol. 17, no. 12, pp. 14 858–14 869, 2012, ISSN: 1420-3049. DOI: 10.3390/molecules171214858. [Online]. Available: https://www.mdpi.com/1420-3049/17/12/14858.

[31] C. Zhang and Z. Li, "A review of lightweight design for space mirror core structure: Tradition and future," *Machines*, vol. 10, no. 11, 2022, ISSN: 2075-1702. DOI: 10.3390/machines10111066. [Online]. Available: https://www.mdpi.com/2075-1702/10/11/1066.

[32] A. Kausar, I. Ahmad, S. A. Rakha, M. H. Eisa, and A. Diallo, "State-of-the-art of sandwich composite structures: Manufacturing to high performance applications," *Journal of Composites Science*,

[33] R. Khan, "Thermo-mechanical properties and applications of glass fiber reinforced polymer composites," *Modern Concepts in Material Science*, vol. 5, Oct. 2023. DOI: 10.33552/MCMS.2023.05.000614.

[34] R. Anusha, O. V. Reddy, and A. Purushotham, "Manufacturing and stress analysis of gfrp and cfrp v-sat antennas," *IOSR Journal of Mechanical and Civil Engineering*, 2024.

[35] C. U. Kiran, M. G. C. Boosa, M. M. V. Lakshmi, and M. M. Swarna, "Electrical characterization of glass fiber reinforced polymer (gfrp) composites for meta surface antenna prospects," *Material Science*, vol. 21, no. 05, 2022.

[36] N. Sharma, T. R. Mahapatra, and S. K. Panda, "Vibro-acoustic analysis of laminated composite plate structure using structure-dependent radiation modes: An experimental validation," *Scientia Iranica*, vol. 25, no. 5, pp. 2706–2721, 2018, ISSN: 1026-3098. DOI: 10.24200/sci.2018.20420.

[37] E. Sather and T. Krishnamurthy, "An analytical method to calculate effective elastic properties of general multifunctional honeycomb cores in sandwich composites," NASA, Tech. Rep. NASA/TM-2019-220275, 2019.

[38] A. Aborehab, M. Abbas, A. Nemnem, and M. Kamel, "Mechanical characterization and static validation of a satellite honeycomb sandwich structure," *Engineering Solid Mechanics*, vol. 9, pp. 55–70, Jan. 2021. DOI: 10.5267/j.esm.2020.5.004.

[39] A. Kumar, N. Muthu, and R. Narayanan, "Equivalent orthotropic properties of periodic honeycomb structure: Strain-energy approach and homogenization," *International Journal of Mechanics and Materials in Design*, vol. 19, Oct. 2022. DOI: 10.1007/s10999-022-09620-x.

[40] E. Carrera, M. Cinefra, E. Zappino, and M. Petrolo, *Finite Element Analysis of Structures through Unified Formulation*. Chichester, West Sussex, UK: Wiley, 2014.

[41] H. D. Chalak, A. Chakrabarti, M. A. Iqbal, and A. H. Sheikh, "Free vibration analysis of laminated soft core sandwich plates," *Journal of Vibration and Acoustics*, vol. 135, 2013. DOI: 10.1115/1.4007262.

[42] J. Wang, C. Wang, R. Chen, and C. Zhang, "Residual Compressive Strength of Aluminum Honeycomb Sandwich Structures with CFRP Face Sheets after Low-velocity Impact," *Applied Composite Materials*, vol. 30, no. 4, pp. 1061–1079, Aug. 2023. DOI: 10.1007/s10443-022-10092-7.

[43] J. Wang, C. Wang, R. Chen, and C. Zhang, "Residual compressive strength of aluminum honeycomb sandwich structures with cfrp face sheets after low-velocity impact," *Applied Composite Materials*, vol. 30, no. 4, pp. 1061–1079, 2023.

[44] Q. Liu, I. Orisamolu, and M. Chernuka, "Consistent finite element discretization of distributed random loads," *Computers & Structures*, vol. 51, no. 1, pp. 39–45, 1994, ISSN: 0045-7949. DOI: `https://doi.org/10.1016/0045-7949(94)90034-5`. [Online]. Available: `https://www.sciencedirect.com/science/article/pii/0045794994900345`.

[45] M. Filippi, M. Petrolo, and E. Carrera, "Refined structural theories for the random response of fiber-reinforced and sandwich composite structures," in *AIAA SCITECH 2022 Forum*. DOI: `10.2514/6.2022-0530`.

[46] ArianeGroup, *Vega-c user's manual*, Issue 0, Revision 0, ArianeGroup, Parigi, Francia, 2018. [Online]. Available: `https://ariane.group/app/uploads/sites/4/2024/10/Vega-C-users-manual-Issue-0-Revision-0.pdf`.